A mechanistic model and experiments on bedrock incision and channelization by rockfall

A. R. Beer[1,2*], J. N. Fischer[2,3], T. P. Ulizio[1], Z. Ma[2,4], Z. Sun[2,5], and M. P. Lamb[2]

[1]University of Tübingen, D-72076 Tübingen, Germany

[2]California Institute of Technology, Pasadena, California 91125, USA

[3]Massachusetts Institute of Technology

[4]University of Illinois Urbana-Champaign

[5]College of Marine Science and Technology, China University of Geosciences, Wuhan 430074, China

*Corresponding author: Alexander Beer (alexander.beer@uni-tuebingen.de)

Key Points:

- Rockfall can erode rocky hillslopes even below the angle of repose
- Grain size has a dominant effect on impact abrasion; slope is of minor importance
- Topographic steering of grains results in self-formed bedrock channels

Abstract

Rockfall and rock avalanches are common in steep terrain on Earth and potentially on other planetary bodies such as the Moon and Mars. Since impacting rocks can damage exposed bedrock as they roll and bounce downhill, rockfall might be an important erosive agent in steep landscapes, even in the absence of water. We developed a new theory for rockfall-driven bedrock abrasion using the ballistic trajectories of rocks transported under gravity. We calibrated this theory using laboratory experiments of rockfall over an inclined bedrock simulant. Both the experiments and the model demonstrate that bedrock hillslopes can be abraded by dry rockfall, even at gradients below the angle of repose, depending on the bedrock roughness. Feedbacks between abrasion and topographic steering of rockfall can produce channel-like forms, such as bedrock chutes, in the absence of water. Particle size has a dominant influence on abrasion rates and runout distances, while hillslope angle is of comparatively minor influence. Rockfall transport is sensitive to bedrock roughness; terrain with high friction angles can trap rocks creating patches of rock cover that affect subsequent rockfall pathways. Our results suggest that dry rockfall can play an important role in eroding and channelizing steep, rocky terrain on Earth and other planets, such as crater degradation on the Moon and Mars.

Plain language summary

Rockfall is common on Earth and other planets. Falling rocks bounce down rocky slopes and likely also erode them. However, it has not been explored how erosive this process is, nor what landforms it might generate. We developed a numerical model for this erosion process and calibrated it with experiments of dry grains hopping down an inclined erodible surface. Both experiments and modeling showed that bedrock erosion from rockfall can happen, even on relatively low-gradient hills. Small hollows were carved by rockfall, which over time coalesced into larger troughs that captured the path of subsequent rocks. This process led to a self-enhancing feedback that produced a bumpy surface with rocky chutes. Rock size had a larger effect on erosion amounts than the steepness of the hill. Our work suggests that dry rockfall can play an important role in the evolution of mountain slopes on Earth and craters on the Moon and other planets.

1 Introduction

Rockfall is a ubiquitous, gravitational-driven process in steep terrain. There is evidence for dry rockfall and rock avalanches on Earth (e.g., Stock et al., 2013), as well as on the Moon and Mars (Bickel et al., 2020a, 2020b; Kumar et al., 2013; Vijayan et al., 2022; Ward et al., 2011; Figure 1A to D). There has been a wealth of research into its preconditioning and cause, both on vertical walls and on mountain slope topography (e.g., Benjamin et al., 2020; D'Amato et al., 2016; Frayssines and Hantz, 2006; Grenon and Hadjigeorgiou, 2008; Matasci et al., 2018; Messenzehl et al., 2017; Wieczorek et al., 1992; Williams et al., 2019). Generally, lithological and exhumation-induced rock fracture, climate, hydrology, and earthquakes are triggers for rock mass release (André, 1997; Collins and Stock, 2016; Guerin et al., 2013; Hales and Roering, 2007; Leith et al., 2014; Mackey and Quigley, 2014; Moore et al., 2009). Also, sediment mass routing following rockfall on steep topography has been accounted for in terms of block-runout and rock avalanching (Dade and Huppert, 1998; Volkwein et al., 2011), in combination with debris flows and fluvial bedload transport (Mergili et al., 2020; Montgomery and Dietrich, 1994; Shugar et al., 2021). Dry rockfall and rock avalanches are typically studied due to their substantial hazard potential. However, they also can be significant agents of erosion, mass transport, and landscape change (Loye et al., 2012; Delannay et al., 2017; Sass and Krautblatter, 2007). Yet, we currently lack mechanistic modeling and experimental constraints on bedrock erosion by rockfall.

Discrete, dry rockfall in physical experiments was shown to erode sloping bedrock surfaces even below the angle of repose (Mokudai et al., 2011; Sun et al., 2021). Rockfall erosion is also supported by observations of boulder tracks (Bickel et al., 2020a, 2020b; Kumar et al., 2013). The impact energy of large rocks that break free from cliffs is substantial (Blackwelder, 1942; Le Roy et al., 2019; Rapp, 1960), and their momentum leads to increased runout distances compared to the smaller grain sizes (Kokelaar et al., 2017; Volkwein et al., 2011). Bedrock abrasion theory suggests that bedrock erosion should scale linearly with impact energy and inversely with the square of rock tensile strength (Beer and Lamb, 2021; Sklar and Dietrich, 2004). So, given abundant rockfall sources in rocky topography, abrasion of bedrock

along the rockfall traverse could be an important process in the topographic evolution of steep terrain (Beer et al., 2019; Sun et al., 2021), despite not being included in most landscape evolution models.

Landforms developed by water-rich rivers and debris flows have received far better study owing to their importance on Earth and they are known to produce channels. In contrast, most previous work on dry granular flows has focused on flow over loose granular substrates, like rock avalanches over talus slopes or grain flows on the front of a sand dune (e.g., Delannay et al., 2017; Selby, 1982). Granular flows tend to spread laterally (Lajeunesse et al., 2004), creating relatively smooth convex lobes, such as grain flows on the avalanche face of a wind dune. The subtle levees and depressions in-between lobes tend to be filled in or diffused away by subsequent avalanches (McDonald and Anderson, 1996). Dry granular flows also tend to cease movement at relatively steep angles of repose, which is around 35-45° for most grains, forming a cone or planar talus slope (Figures 1E and G; Delannay et al., 2017; Kirkby and Statham, 1975; Sass and Krautblatter, 2007; Selby, 1982). Similar angles for dry granular flow deposits have been measured on Mars (Atwood-Stone and McEwen, 2013; Dickson et al., 2007). The generally smooth and steep topography from dry flows over loose substrates contrasts sharply with the channel-like landforms developed in some steep rocky terrain, such as bedrock chutes (Figures 1C and D; Ward et al., 2011). This contrast has fueled the idea that water is needed to develop channelized forms, particularly at slopes less than the angle of repose for dry avalanches (e.g., Howard, 2007).

The mechanics of how flowing water produces channels is relatively well understood. Water follows the steepest slope, such that the topography funnels the flow, causing erosion rates to increase, which, in turn, causes further channelization (Horton, 1945). It is unclear if a similar feedback can occur for dry rockfall. While dry granular flows can be focused down pre-existing topography (Pelletier et al., 2008), dispersive pressures due to grain-grain and grain-bed collisions cause granular flows to spread laterally (e.g., Lajeunesse et al., 2004; Figure 1G), rather than to focus and entrench. However, Sun et al. (2021) showed in an experiment that dry rockfall traversing a bedrock substrate can form channelized landforms. The strong substrate allowed for persistent topographic forms over many rockfall events, which steered rockfall into preferred pathways. Thus, similar to fluvial incision, rockfall was funneled into proto-channels, enhancing erosion there (Figure 1H) and allowing for further entrenchment. Another experiment that produced chutes by dry flows used a very light and fine-grained sediment substrate under high humidity, which provided cohesive strength between grains (Shinbrot et al., 2004). Rockfall over a relatively smooth bedrock substrate can traverse relatively low-sloping terrain due to low friction angles (DiBiase et al., 2017; Sun et al., 2021), which may help explain channel-like landforms below the angle of repose on the Moon and Mars in the absence of water (Conway et al., 2015; Dickson et al., 2007; Heldmann and Mellon, 2004).

Here we develop theory and a numerical model for abrasion by rolling and bouncing rocks over a bedrock bed in order to better understand the role of rockfall in landscape denudation and landform development. We calibrated and evaluated the model against physical experiments of dry rockfall traversing a planar and tilted bedrock slope, where we used polyurethane foam as a bedrock simulant, similar to Sun et al. (2021). We used the model to

answer whether rockfall can form channelized landforms, and the effect that hillslope angles and rockfall sizes have on rockfall erosion rates.

2 Dry Grain Abrasion Model (DGAM)

2.1 Grain trajectories

We develop a dry grain abrasion model (DGAM), which tracks discrete rockfall events, including grain trajectories and abrasion over a gridded 2.5D digital elevation model (DEM with no 3D overhangs), built out of X, Y, Z-coordinates with slopes θ_{cell} [°] and cellsize d_{cell} [m] (setup in Figure 2A; scheme and workflow in the Supplemental Information and Table S1; see notation section). For simplicity, we model only one rockfall grain size and set d_{cell} equal to the grain diameter d_{grain} [m]. Each grain of mass m_{grain} [kg] is released from the upstream boundary of the model domain with initial variable values (grain deflection velocity, $v_{out,0}$ [m/s], absolute grain deflection angle, $\alpha_{out,0}$ [°], and grain hop length, $l_{hop,0}$ [m]), in one of the D8 grid directions (parameter ξ_0; i.e. deflection to all adjacent neighbor cells). By having these variables drawn from an intended distribution, this procedure ensures controllable randomness to the first impacts.

Inside the model domain, grains hop over multiple cells following classical mechanics (ballistics) along a tilted plane. For a defined grain impact cell i (with coordinates X, Y, Z_i), we calculate the incoming grain's trajectory from its original deflecting cell (X, Y, Z_{i-1}) as grain hop length $l_{hop,i-1}$ along the direction ξ_{i-1}, as the distance between both cell's coordinates (ΔXY is the horizontal distance, and ΔZ is the vertical distance between both cells)

$$l_{hop,i-1} = \sqrt{\Delta XY^2 + \Delta Z^2} \quad (1)$$

The hop time, $t_{hop,i-1}$ [s], of this trajectory is based on the grain's original deflection variables $v_{out,i-1}$ and $\sin \alpha_{out,i-1}$, as well as on gravitational acceleration, a_{grav} [m/s^2]:

$$t_{hop,i-1} = v_{out,i-1} \sin \alpha_{out,i-1} + \frac{\sqrt{(v_{out,i-1} \sin \alpha_{out,i-1})^2 + 2 a_{grav} \Delta Z}}{a_{grav}} \quad (2)$$

Grain velocity at the cell impact, $v_{in,i}$ [m/s], and grain impact angle, $\alpha_{in,i}$ [°], then are:

$$v_{in,i} = \sqrt{(v_{out,i-1} cos\alpha_{out,i-1})^2 + (v_{out,i-1} sin\alpha_{out,i-1} - a_{grav} t_{hop,i-1})^2} \quad (3)$$

$$\alpha_{in,i} = arcsin \frac{v_{out,i-1} cos\alpha_{out,i-1}}{v_{in},i} \quad (4)$$

After an impact (i.e., along the next trajectory direction, ξ_{i+1}), the grain trajectory follows a probabilistic direction-sampling based on weighted downslope gradients in the proximity of the impact cell (DiBiase et al., 2017; Dorren et al., 2004). This procedure is intended to account for natural stochasticity of the rebounds due to grain inertia, grain shape, and surface roughness (cf. Volkwein et al., 2011).

The model can be operated in two modes to assess frictional losses due to impacts with the bed. In the pure grain hop mode (mode I), grain kinetic energy loss from impacts is expressed in grain velocity reduction by means of a shock term, κ_{shock} [1/m] (Quartier et al., 2000),

$$v_{out,i} = v_{in,i} - \kappa_{shock} v_{in,i}^2 \Delta t \quad (5a)$$

with $v_{out,i}$ [m/s] is the deflection grain velocity, and Δt [s] is an impact time, which we assume to be *0.1* s (DiBiase et al., 2017; Gabet and Mendoza, 2012). In mode II, impact energy loss also includes sliding and rolling friction based on a modified Coulomb friction law (DiBiase et al., 2017; Gabet and Mendoza, 2012),

$$v_{out,i} = v_{in,i} - a_{grav}\left(\sin \Theta_{cell,i} - \tan \Phi_{surf,i} \cos \Theta_{cell,i}\right) - \kappa_{shock} v_{in,i}^2 \Delta t \quad (5b)$$

which includes the dynamic surface friction angle, $\Phi_{surf,i}$ [°] between grains and the surface, accounting for microtopography. Following previous work (DiBiase et al., 2017; Gabet and Mendoza, 2012), we treat this slope as an exponential probability distribution

$$\Phi_{surf,i} = \arctan\left(\frac{1}{\tan \bar{\mu}_{surf}} e^{-\frac{\tan \mu_{eff}}{\tan \bar{\mu}_{eff}}}\right) \quad (6)$$

of the effective friction angle μ_{eff} [°]. The grain's deflection angle $\alpha_{out,i}$ [°] is assumed to be the reflection angle of $\alpha_{in,i}$ on the local cell slope $\theta_{cell,i}$ [°] in direction ξ_i

$$\alpha_{out,i} = \alpha_{in,i} - 2\theta_{cell,i} \quad (7)$$

The location of the next impact (X, Y, Z_{i+1}) then is determined by an iterative process. The grain's trajectory heights Z_{traj} [m] are calculated relative to the traversed cell boundaries $Z_{cell.boundary}$ [m] along the grain's trajectory direction ξ_i

$$Z_{traj} = tan\alpha_{out}(n_{cells} + 0.5)\frac{d_{cell}}{2} - \frac{a_{grav}}{2v_{out,i}^2 cos_{\alpha_{out,i}}^2}\left(\frac{d_{cell}}{2}\right)^2 \quad (8)$$

for a number of n_{cells} until $Z_{traj} < Z_{cell.boundary}$. Then (X, Y, Z_{i+1}) is defined as the last cell that could not be traversed by the grain, and $l_{hop,i}$ is calculated in between (X, Y, Z_i) and (X, Y, Z_{i+1}) (Equation 1). The grain's hop height $h_{hop,i}$ [m] is the maximum of the vertical distances between traversed cell boundaries and trajectory heights, i.e. $\max(Z_{traj} - Z_{cell.boundary})$. The trajectory procedure is repeated until the grain leaves the model domain or comes to rest (Table S1). If a grain has too low deflection velocity, $v_{out,}$, or too low deflection angle, α_{out}, to cross the next cell boundary, it is deposited at the current cell. We assume a resting particle is subsequently set in motion from being hit by a mobile grain, drawing randomly from the grain entrance variable values discussed above. However, if a grain is in a depression with neighboring cells higher than two grain sizes, we assume the grain stays there and acts as cover that protects the bedrock from abrasion.

2.2 Bedrock abrasion and morphodynamics

The amount of bedrock abrasion of a cell, $w_{cell,i}$ [m], due to a single grain impact is calculated as:

$$w_{cell,i} = k_{ero}\frac{0.5 m_{grain} {v_{in,n,i}}^2}{d_{cell}^2} = k_{ero}\frac{\varepsilon_{kin,n,i}}{d_{cell}^2} \quad (9)$$

$$v_{in,n,i} = \cos \theta_{cell,i}\, v_{in,i} sin\alpha_{in,i} \quad (10)$$

based on a bedrock erosion efficiency factor, k_{ero} (i.e., grain erosivity, [m^3/J]). To conserve mass, the erosion amount, $w_{cell,i}$, is assessed in the vertical direction since the cell area in our calculations is measured on a horizontal grid. The surface-normal component of the kinetic impact energy, $\varepsilon_{kin,n}$ [J], results from the surface-normal component of the grain impact velocity, $v_{in,n}$ [m/s]. The velocity component accounts for impact-induced fracturing causing wear, instead of surface-parallel gouging (cf. Sun et al., 2021). For steeper slopes, its value decreases compared to the approximation of a vertical impact velocity that is commonly used in fluvial abrasion theory (Beer and Lamb, 2021; Beer and Turowski, 2021; Engel, 1978; Sklar and Dietrich, 2004). While the actual geometry of the impact event depends on local parameters like grain shape and bedrock roughness that are not explicitly included in the model, the model is calibrated with experiments (below) and thus these local geometric effects are incorporated into the empirical model parameters.

The DGAM model allows the user to switch off abrasion (Equation 9), since it is decoupled from frictional losses (Equation 5). This option enables process-independent model assessment like varying grain sizes or hillslope angle. Accounting for abrasion (Equation 9) results in evolving hillslope topography that influences grain impact energy ε_{kin} (via modified hop time t_{hop}, which drives impact velocity v_{in}; Equation 3), and alters the local slope gradient around each cell. This again affects the subsequent direction of deflecting grains (parameter ξ), which can result in topographic steering feedback. Application of the model requires inputs of initial grain entrance variables ($v_{out,0}$, $\alpha_{out,0}$ and $l_{hop,0}$) and the bedrock erosion factor, k_{ero}, per model cell. The grain impact shock term, κ_{shock}, is calibrated as described below, but could be adjusted for specific situations (e.g., varying grain shape).

3. Experimental Setup and Model Application

We conducted two sets of experiments (Table 1) to generate grain trajectory and abrasion data, and used this data to calibrate the DGAM model. The first set consisted of five large-scale experiments with an erodible foam substrate that evolved during the experiments due to abrasion from dry rockfall. We refer to these as *erodible-bed experiments* (EB). The erodible-bed experiments had different inlet conditions, hillslope gradients, and particle sizes to test the model performance relative to these variables. The experiments of the second set were of smaller scale, did not vary the inlet nor erode the bed, and were used to evaluate grain trajectories as a function of bed slope. We refer to these as *fixed-bed experiments* (FB).

3.1. Erodible-bed experiments

We ran five erodible-bed experiments (*EB*, Table 1; more details in Table S2). These experiments were not designed to replicate or reproduce particular rockfall and hillslope topography, but to provide data on grain trajectories, bedrock abrasion, and morphodynamic feedback for model comparison. Erodible-bed experiment 1 (i.e., *EB1*) was conducted using a 2.2 m long, 0.76 m wide test section using large river cobbles on a relatively shallow sloping bed ($\theta_{slope} = 16.7°$). The detailed experimental setup and some results from experiment *EB1*

were previously described in Sun et al. (2021). These observations include the ability of rockfall to run out over low gradients and to focus, resulting in channelized landforms through topographic steering. Here, we use data from *EB1* to help evaluate DGAM and to compare results from four additional erodible-bed experiments and six fixed-bed experiments, as detailed below.

The four new erodible bed experiments (*EB2* – *EB5*) were conducted in a different but comparable facility as *EB1*. We used a tilting flume, $4.5\ \mathrm{m}$ long and $0.65\ \mathrm{m}$ wide, filled with a block of smooth, homogeneous polyurethane (PU) foam, which acted as a highly-erodible substitute for bedrock (Scheingross et al., 2014; Figures 2B, C). Each experiment (including *EB1*) used the same type of foam with a density of $0.06\mathrm{t/m^3}$, a tensile strength of $\sigma_{foam} = 0.32\mathrm{MPa}$, and a Young's Modulus of $3.92\mathrm{MPa}$. This foam has been shown previously to produce realistic erosional morphologies through abrasion by grain impacts in both air and water (Scheingross et al., 2014; Sun et al., 2021). Moreover, the foam erodibility follows the same scaling law with tensile strength as bedrock, supporting it as an experimental analog to natural rock (Beer and Lamb, 2021; Lamb et al., 2015). The erodibility framework holds over several orders of magnitude both in impactor energy and impact abrasion (Beer and Lamb, 2021), indicating that these laboratory experiments can be scaled to natural cases of larger impact energies and real bedrock using the relative erodibilities in a scaling factor.

The variables that changed between our experiments were the inlet design for the grains to enter the flume, grain size/shape properties, and the flume slope (Table 1). Experiment *EB1* used rounded granitic grains (density of $2.75\ \mathrm{t/m^3}$) with a median grain diameter of $d_{grain} = 0.061\mathrm{m}$; experiments *EB2-EB4* used medium-sized and rounded andesitic grains ($d_{grain} = 0.023\mathrm{m}$ and $0.03\mathrm{m}$, respectively; grain density of $2.33\mathrm{t/m^3}$; Figure 2D); and *EB5* used $0.015\mathrm{m}$ angular granite grains. The initial slope of the planar foam bed was $\theta_{slope} = 16.7°$ for *EB1*, $19.5°$ for *EB2-EB4* and $35.0°$ for *EB5*. The inlet for rockfall spanned the width of the flume for experiments *EB1, EB2* and *EB5*, but was constricted to $0.2\mathrm{m}$ width in the flume-center for experiments *EB3* and *EB4* (Table S2).

The experiments were designed such that the surface friction angle of the grains on the foam Φ_{surf} [°] was similar to the slope Θ_{slope} of the planar foam bed at the beginning of the experiment (Table 1). This design was intended to allow grains to be intermittently mobile even when patches of static grains were deposited on the bed. The grain's pocket friction angle, Φ_{pocket} [°] (corresponding to the angle of repose of a grain pile) was measured following previous work (Prancevic and Lamb, 2015; Sun et al., 2021), whereby we glued grains of like size and angularity on a planar board. Then a loose grain was placed on this surface, the board was slowly tilted until the grain was mobilized, and the tilting angle was reported as the pocket friction angle. The process was repeated for ~100 different grains selected at random and placed at random on the board. We also repeated this process for grains placed on the planar foam board, which we report as the mean surface friction angle, Φ_{surf} [°]. Grains should be highly mobile when their friction angle is lower than the topographic slope (DiBiase et al., 2017), which was the case for all of our experiments with grains traversing the smooth foam bedrock. However, this mobility transiently changed during the experiments due to the growth of topographic bedrock roughness and due to static patches of grains that were more difficult

to traverse (i.e., $\Phi_{pocket} > \Phi_{surf}$; Table 1). Although we achieved high mobility in the experiments through relatively round grains and smooth foam topography, low surface friction angles are also expected in natural settings with angular rockfall grains that are much larger than the bedrock topographic roughness (DiBiase et al., 2017; Sun et al., 2021). In other words, modeling multi-meter scale boulders in the laboratory is not feasible, so we created similar particle dynamics by lowering the surface friction angle through particle roundness rather than by larger grain size.

Each experiment started with a new block of planar, smooth foam (Figure 2C). Dry grains were introduced at the upslope end of the flume at a steady rate from an auger sediment feeder. The feed rate was slow enough ($250 - 1'550$ grains/minute), so grains entered and traversed the flume individually, with minimal grain-grain interactions. Particles traversed a board with pegs spaced at 0.05m to spread the grains across the inlet. The flume had rigid vertical walls that reflected grains towards the center of the test section, mimicking grains exiting and entering the domain under an infinitely wide scenario. Each experiment lasted for several hours of runtime, in which $5 - 22$ t of sediment traversed the test section (Table 1; details in Table S2).

Grain trajectories were recorded using high-speed cameras with fisheye lenses (GRASHOPPER, set to 160 frames/s) at three lateral positions along the flume (Figure 2B) and one camera from top. We rectified and cut the distorted fisheye-lens pictures, converted them to black and white, and scaled their dimensions by scale bars attached to the flume walls in the photos. Then we applied particle imaging velocimetry (PIV) to measure grain trajectories using Python-based software packages (OpenCV and TrackPy; Python, 2021) and calculated grain trajectory metrics. For the side-view cameras, these metrics were grain impact and deflection velocities (v_{in} and v_{out}), impact and deflection angles (α_{in} and α_{out}), hop heights, and hop lengths (h_{hop} and l_{hop}; Figure 2B; Table 1; Table S2), which we calculated perpendicular to the foam surface from grain traces through subsequent pictures. We only used complete grain trajectories showing several hops, but discarded incomplete trajectories, photos with unclear grain detection from the black-white conversion, and photos comprising several grains. For the top camera, we only calculated the lateral and downslope (X, Y) coordinates of the trajectories, as we could not detect the actual impact positions.

We surveyed the evolving foam bed topography approximately every one to two hours in each experiment. During this time, we stopped the particle feed and removed any accumulated foam dust using compressed air. The foam surface was surveyed from two positions above the flume using a terrestrial laser scanner, TLS (FARO FOCUS 3D), which delivered 3D pointclouds (i.e., X, Y, Z-coordinates) with a mean spatial resolution of ~1 mm. The individual, subsequent TLS-measured pointclouds were co-registered on the initial smooth surface using twelve fixed target points along the flume walls (0.1m-diameter wooden spheres, which allowed for calculating their centers; Figure 2B and 2C). Vertically differencing the co-registered pointclouds using the M3C2 algorithm in cloudcompare software (CloudCompare, 2022; Lague et al., 2013), we calculated transient spatial foam abrasion and also noted the total abrasion volume (i.e., total abrasion amount over the whole flume surface; V_{flume} [m^3]).

3.2 Fixed-Bed Experiments

The fixed-bed experiments (*FB*) were designed to gain more data on grain hop trajectories but using a simpler setup than the erodible-bed experiments. The experiments used a tilting chute that was 1.1 m long and 0.1 m wide. Six experiments were conducted (*FB1-FB6*), each with identical parameters except that the flume bed slope, Θ_{slope},was varied between $20°$ and $45°$ (Table 1; lower part). The experiments used the same rounded andesite gravel as experiments *EB3* and *EB4*. The flume bed consisted of the same foam as in the erodible-bed experiments, but since it was only traversed by a hundred grains over time, abrasion was negligible, and the topography remained planar. Grains were fed into the chute individually by hand. A high-speed lateral-view camera (the same as described above) was used to capture grain trajectories, and grain trajectory analysis was the same as in the erodible bed experiments.

3.3. Comparing the Model to Experiments and Natural Cases

As we want to verify the dry rockfall abrasion theory to represent a feasible hillslope erosion process, we (i) calibrate the DGAM model to reproduce the experimental observations of the EB and FB, then (ii) explore grain trajectories and abrasion varying hillslope angle and rockfall grain size, and finally (iii) scale the model to predict natural hillslope topography.

To run the model for the experimental setups, grain reflection from the flume walls was accounted for by stopping a grain's trajectory on the last cell in front of the wall. From there, it starts a new trajectory with its given variables but in a new direction ξ. Mean foam abrasion per grain impact, V_{cell} [m^3], for an experiment of a given flume slope and grain type (Table 1) was calculated as:

$$V_{cell} = \frac{V_{flume}}{n_{grains,tot}\, n_{imp,tot}} = \frac{V_{flume}\, m_{grain}\ l_{hop}}{m_{grains,tot}\, l_{flume}} \tag{11}$$

by estimation of the number of grains used, $n_{grains,tot}$ [-] (i.e., the total sediment mass fed into the experiment, $m_{grains,tot}$ [kg], divided by a single grain's mass, m_{grain}), and the mean number of impacts per grain along the flume, $n_{imps,tot}$ [-] (i.e., flume length, l_{flume} [m], divided by mean grain hop length, l_{hop}). To convert the experimental results into the grid world of the DGAM model, we assumed this abrasion volume is equally distributed over a model cell that is impacted by a grain (i.e. $V_{cell} = w_{cell}\, d_{cell}^2$, with $d_{cell} = d_{grain}$, as defined above). This assumption is reasonable, given the observation of generally platelet-shaped bedrock fragments abraded from grain impacts (Beer and Lamb, 2021). We then scaled the grain erosivity factor, k_{ero}, as the fraction between V_{cell} and the surface-normal component of the grain's mean kinetic impact energy, $\varepsilon_{kin,n}$ (Equation 9).

Using the calculated k_{ero} values and the measured initial grain entrance variables ($v_{out,0}$, $\alpha_{out,0}$ and $l_{hop,0}$) for each erodible-bed experiment *EB* (Table 1, upper part), we iteratively fit the DGA model (mode I, i.e. pure grain hopping) shock term coefficient, κ_{shock}, to

best reproduce the means of the observed grain trajectory variables and foam surface abrasion rates of the experiments.

Having calibrated the model, we used it to explore the rockfall transport and impact abrasion over a range of natural hillslope angles ($5 < \Theta_{slope} < 45$) and grain sizes ($0.1\text{m} < d_{grain} < 1\text{m}$).To model dry rockfall abrasion on rocky hillslopes under natural scenarios of hillslope angle, grain sizes and lithology, we scaled the bedrock abrasion rate (V_{cell}) according to the rock tensile strength following

$$V_{rock} = V_{cell}\left(\frac{\sigma_{foam}}{\sigma_{rock}}\right)^2 \quad (12)$$

where V_{rock} [m^3] is the volumetric abrasion for any bedrock cell of tensile strength σ_{rock} (Beer and Lamb, 2021; Scheingross et al., 2014).

4. Results

4.1 Topographic evolution in the experiments

All five erodible-bed experiments (*EB*; Table 1, upper part) evolved in a similar pattern, and the final bed topographies resembled each other (Figure 3B). Here, we describe the general evolution of these experiments to document the dry abrasion process, using *EB5* as an example (Figure 3A). Grains discretely hopped down the foam surface and abraded it by incremental impact abrasion, resulting in tiny pit craters and abraded foam dust creating lasting topography (cf. Figure 1H). Initial grain abrasion pits down the entrance transiently grew into larger hollows from ongoing impacts of subsequent grains (Figure 3A, left panel, shown for *EB5*), although separate hollows were less distinct for the largest grains used in *EB1*. Grains leaving these hollows initiated faint (mm-deep), parallel rills down the slope. Reaching a depth of around one grain diameter, these hollows laterally coalesced into a trough, and the rills further evolved (Figure 3A, central panel). This process is portrayed by the temporal evolution of the lateral profiles through the hillslope (Figure 4A, upper panel). Over time, the rills extended in depth and converged downslope into a central main channel (Figure 3A, right panel; Figure 4A, lower panel). This channel's long profile maintained a slight bumpiness over time (Figure 4D), arising from the subsequent evolution of new troughs, whose rims transiently traversed downslope (Figure 3A, right panel). This pattern emerged in all erodible bed experiments (Figure 3B).

Throughout the experiments, some grains came to rest, though they were soon hit by mobile grains and remobilized. So, permanent spatial cover generally did not occur on the main foam board, even at the lowest experimental slope of $\Theta_{slope} = 17°$ (*EB1*; Table 1). However, when a topographic depression (as the upper trough) reached a depth of two grain sizes relative to its downslope rim, it gradually got clogged by resting grains, which formed a stationary cover in the depression. Subsequent grains laterally traversed this patch of grains and funneled into the evolving main central channel, uniting the former rills downslope (Figure 3A, right panel); a similar sequence was described for *EB1* by Sun et al. (2021). Due to the focusing of the grains into the central trough, lateral parts of the foam surface experienced

a decreasing number of grain impacts over time (Figure 4B), and they gradually abraded slower (Figure 4C; shown here is vertical abrasion equivalent to w_{cell}, for comparison). This morphodynamic feedback resulted in a channelized hillslope for all erodible-bed experiments, independent of hillslope angle or grain size (Figure 3B). The current pattern of the abrasion measurements therein reflected the current surface topography, e.g., the eroded rills (Figure 4C upper panel vs. Figure 3A central panel).

When the patch of static grains in the upper trough initiated, it grew laterally and in height due to the higher pocket friction angle of the grain patch relative to the foam board (cf. Table 1). Once this grain pile backed up onto the peg board, the experiment was terminated (Figure 2B). Without the upslope limitation of the experimental facility, the grains probably would have continued piling until reaching their pocket friction angle, resulting in a grain avalanche, followed by a subsequent pile-up, and so on. Final bedrock topographies typically consisted of an upslope trough filled with a static grain patch, with a channel that extended and became less defined downslope (Figure 3B and Figure 4D; shown after sediment cover patch removal).

Changing the grain inlet width for the erodible-bed experiments (flume-wide for *EB1*, *EB2,* and *EB5*, central for *EB3* and *EB4*; Table S2) dictated the lateral extend of the upper trough (Figure 3B). The larger the grain size of the experiment, the farther the trough extended downslope (cf. *EB1* vs. *EB5*). Regardless of inlet width or particle size, all experiments showed a smooth rim at the trough outlet, followed by rills and a subsequent emerging trough, which initiated a channel (Figure 3A and Figure 4D).

4.2. Grain trajectories and model calibration

On average, for the erodible-bed experiments *EB1-EB3 and EB5* (for *EB4,* there were too few measurements available for robust statistics), grains hopped by $\bar{l}_{hop} = 0.19 \pm 0.11$ m at $\bar{h}_{hop} = 0.02 \pm 0.02$ m height (mean and standard deviation) (Figure 5, grey boxplots; Table S2). They impacted at angles of $14 \pm 14°$ above the respective foam surface (i.e., $\bar{\alpha}_{in} - \Theta_{slope}$). The grain's hop lengths, hop heights, and impact angles were insensitive to the hillslope angle. However, the mean impact velocities, $1 < \bar{v}_{in} < 2$ m/s, increased with steeper hillslope angles. Deflection angles and deflection velocities generally equaled their impact pendants, so little kinetic energy was lost by the impacts. Mean initial grain entrance velocity from the peg board was around $v_{in,0}$ = 1.1 m/s in the erodible-bed experiments. In the fixed-bed experiments, these velocities were higher (~1.5 m/s), resulting in increased hop lengths, impact angles, and impact velocities (Figure 5, white boxplots).

Derived vertical grain impact abrasion volumes per cell area, w_{cell} (i.e. $V_{cell}/\, d_{cell}^2$; cf. Equation 11) in the order of µm decreased with increasing slope angle (Figure 6A). This pattern is consistent with impacting grain's grain erosivity, k_{ero} (i.e. V_{cell} / $\varepsilon_{in,z}$), with some uncertainty for smaller, rounded grains of low erosivity, while even smaller but angular grains maintained their erosivity even for low impact energies (*EB5*; Figure 6B; Table 1). Normalizing k_{ero} values by grain cross-sectional area or cell size, ${d_{grain}}^2$, resulted in an erosivity measure that collapsed the data of the fixed-bed experiments with round grains (*FB1-FB4*) around 0.001, while for the

435 angular grains, it remained higher (k_{ero}/d_{grain}^2= 0.003m/J; Figure 6C; Table 1). These values can
436 be used to calculate the DGA model's k_{ero} factor for a given grain size.

437 To calibrate the model using the experiments, we set k_{ero} based on the observed
438 erosion amounts (Figure 6B). Next, we kept the observed initial grain entrance variables ($v_{in,0}$,
439 $\alpha_{out,0}$ and $l_{hop,0}$) fixed in the model and varied the shock term coefficient, κ_{shock}, to best
440 reproduce the suite of the mean trajectory parameters for each erodible-bed and fixed-bed
441 experiment. Comparing the predicted versus the modeled means of the grain trajectory
442 parameters l_{hop}, $v_{in,z}$, α_{in}, and V_{cell} (the latter parameter only for the erodible-bed
443 experiments), we identified experiment-specific κ_{shock} values with the first closest general
444 agreement (Figure 7 for EB2; cf. Figure S1 for all experiments). All these identified values fell in
445 a narrow range around $\kappa_{shock} = 0.8$ m^{-1}.
446

447 **4.3. Model and experimental comparison**

448 Predictions from the κ_{shock}-calibrated model generally fit the pattern of the measured
449 PIV-derived trajectory parameters along the flume, though the range of the predictions was
450 much lower (mean deviation -15% and range -60% for *EB2* in Figure 8). The largest deviations
451 existed for the predicted grain hop length, l_{hop} (-65%, Figure 8A), and the deflection velocities
452 (-15%, Figure 8D), both mainly further downslope of the flume. Both grain impact and
453 deflection angles were overpredicted at the flume's entrance. The impact angle, α_{in}, soon
454 matched the observations, but the deflection angle, α_{out}, remained increased (6%, Figure 8E-F).
455 Overall the grain impact velocities were met (-5% deviation, Figure 8B, C) and thus also the
456 initially relatively increased impact abrasion fit the calculated values along the flume (-5%,
457 Figure 8G).

458 All grain trajectory parameters for a fixed grain size increased with a steeper hillslope
459 angle (Figure 9A; for d_{grain} = 0.03m). Over the range of $\Theta_{slope} = 20°$ to $45°$ hop length and
460 impact velocity doubled, while impact angles remained more constant relative to the surface
461 slope (Figure 9A; upper three panels). The resulting abrasion volume remained within one order
462 of magnitude for volumetric impact abrasion, V_{cell}, and also for local erosivity (i.e., abrasion per
463 meter downslope, V_{cell} / l_{hop}; Figure 9, two lower panels). DGAM-predictions over $\Theta_{slope} =$
464 $5°$ to $45°$ for both round grains (d_{grain} = 0.03m, representative for *EB3*, *EB4*, and *FB1-FB6*) and
465 for angular grains (*EB5*) followed the general trends, in which angular grains consistently
466 underpredicted observed abrasion volume (V_{cell}; Figure 9A, two lower panels).

467 In contrast to the influence of slope angle, grain trajectory parameters showed more
468 sensitivity to increasing grain size when holding slope fixed (Figure 9B; for Θ_{slope} = 35°). Over
469 the range of $d_{grain} = 0.015$ to 0.036m hop length, impact velocity, and impact angle all
470 doubled (upper three panels of Figure 9B). Grain impact abrasion and local erosivity increased
471 nonlinearly with grain size following a strong trend (two lower panels of Figure 9B; impact
472 abrasion was not measured for *FB4*, but the predicted value from the measured impact
473 energies was comparable to *EB5*). Accordingly, and from a general perspective of natural
474 hillslopes, rocky surfaces with slope angles ranging from $\Theta_{slope} = 15°$ to $45°$ and impacted by
475 rockfall grains of $d_{grain} = 0.01$m to 1.00m diameter may experience local impact abrasion

476 volumes spanning six orders of magnitude (Figure S2; calculated using the erosivity for angular
477 grains, as in *EB5*; Figure 6B, C). Herein, the influence of slope angle is inferior as compared to
478 grain size. The abrasion volumes predicted for laboratory foam can be scaled to abrasion
479 volumes of any (massive) bedrock by the inverse square of the material's tensile strengths
480 (Equation 13).
481
482 **4.4 Model exploration**

483 Having calibrated the model, we sought to explore the impact of the upstream
484 boundary condition on bedrock landforms developed by rockfall. For this, we simulated
485 topography evolution from an initially smooth, sloping plain, similar to the experiments, with
486 rockfall fed in from the top of the domain. We set the DGAM parameters to be more realistic
487 for natural cases, including larger, angular rockfall grains ($m_{grains,tot} = 800\text{tons}$ of $d_{grain} =$
488 0.20m) on a steep granite hillslope ($\Theta_{slope} = 35°$; $\sigma_{rock} = 5\text{MPa}$, cf. Equation 12; $k_{ero} =$
489 0.003m/J, cf. Figure 6C, C; κ_{shock} = 0.8m^{-1}, cf. Figure 7). All other parameters were set as in *EB2*
490 (Φ_{surf}, grain density, $v_{out,0}$, $\alpha_{out,0}$ and $l_{hop,0}$). We conducted two numerical experiments with
491 all parameters equal except for a change in the feed of rockfall: Uniform feed over the center of
492 the model domain (cross-sections in Figure 10A, long profile in Figure 10C) vs. rockfall dispersed
493 over three source areas (Figure 10B and D).

494 For the case of a uniform central rockfall entrance, the initially planar hillslope surface
495 developed a deepening trough at the entrance, which sourced into a channel with decreasing
496 depth further downslope (panels of Figure 10A; more panels in Figure S3A). This process was
497 driven by steering of grains into the channel center, increasing abrasion there (transient lateral
498 grain distribution in the third panel of Figure 10A; cf. grain trajectories and local impact
499 abrasion in Figure S3C and E). Down the hillslope, the hopping grains produced a sequence of
500 intermittent and downslope-wandering concave troughs and convex rims of decreasing size,
501 comparable to the topographic slope evolution during the experiments (Figure 10C vs. Figure
502 4D). The experiment ended when the upper trough reached a depth of one grain diameter
503 relative to its downslope rim, capturing all subsequent grains.

504 Modeling with the same number of grains as before, but fed onto the hillslope in three
505 separated inlets (Figure 10B; more cross-sections shown in Figure S3B), resulted in comparable,
506 but smaller concave-shaped channels downslope, i.e., in parallel rills that started coalescing.
507 This experiment also stopped due to over-deepening of the upper trough (Figure 10D), after a
508 remaining wider lateral grain distribution and abrasion than in the other experiment
509 (Figure 10B third panel; Figure S3D and F).
510

511 **5 Discussion**

512 **5.1 Model calibration and validation**

513 It is currently not possible to compare our model predictions to natural erosion rates
514 because the model requires specification of rockfall frequency, rock size and bedrock strength,
515 which are generally unknown. Ultimately, a complete model of landscape evolution by dry
516 rockfall will need to incorporate these rockfall generation processes, which can then be coupled

to model rockfall abrasion. Due to the lack of field constraints, we turned to scaled laboratory experiments to test the model. By varying hillslope angle, grain size, and grain shape, we calibrated a cellular, dry grain trajectory abrasion model by means of grain shape erosivity and an impact shock term, κ_{shock} (DGAM; Figures 2, 6 and 7). The grain trajectory velocities, angles, and hop length only varied within their magnitude in our *EB* flume experiments and they showed a larger spread for the *FB* due to a small test population of some tens of grains (Table 1 and Table S2; Figure 5 and Figure 8). The calibrated model did not entirely reproduce these measured grain trajectories (fewest the hop length; Figure 8), which may be attributable to the larger range of the experimental trajectory variables due to uneven grain shape (Figure 5). Varying the impact shock term, κ_{shock}, could account for this discrepancy by generating a wider distribution of trajectories. Grain shape likely has a nonlinear influence both on grain mobility (angular grains have large pocket and surface friction angles; Table 1; Figure 9) and on grain impact erosivity (angular grains will be more erosive; Neilson and Gilchrist, 1968). Though, summed impacts of a given grain shape mixture may cancel out varying abrasion volumes of different grain shapes, as indicated by the general collapse of experimental abrasion data for local impact abrasion (Figure S4D-F). This leveraging is also reflected in the deviation of model-predicted lower deflection velocities but higher deflection angles that still led to acceptable abrasion rates based on a fixed shock term (Figure 8D, F, and G).

5.2 Effect of slope and grain size

Constraining grain impact abrasion volume is a crucial factor in the process, and grain size showed to be of dominant influence compared with hillslope angle (Figure S2). Modelled trajectory parameters increased modestly with increasing slope angle, and abrasion volume only rose by one order of magnitude from shallow to steep slopes (Figure 9A). All parameters also increased with larger grain size (Figure 9B). Importantly, grain impact erosivity nonlinearly rose, spanning six orders of magnitude from pebbles to 1m boulders (Figure 9B lower panels and Figure S2) due the nonlinear impact energy-dependence on grain diameter cubed (cf. $m_{grain} = \sigma_{rock}\frac{4}{3}\pi(\frac{d_{grain}}{2}))^3$). This matches the high erosivity of large (meter-sized) rockfall boulders analyzed in rockfall runout studies (Bickel et al., 2020a, 2020b; Volkwein et al., 2011) and in previous abrasion experiments (Mokudai et al., 2011), and matches their importance in fluvial abrasion (Beer and Lamb, 2021; Turowski et al., 2015).

Within a distribution of rockfall grain sizes, the largest grains will have an immediate effect on surface morphology since both subsequent grain trajectories will be more influenced by their erosive impact on surface roughness, and their momentum-dependent runout distance is the largest (Kokelaar et al., 2017). Though, the actual/transient grain size distribution will determine the representative grain size that may be applicable for average modeling. Field data on individual (caprock) rockfall grain size distributions are lacking to our knowledge, though it could, e.g., be derived from rocky hillslope's fracture-spacing (Neely and DiBiase, 2020) and then allow assessment of the interplay between rockfall erosivity and slope erodibility.

5.3 Effect of substrate strength

As grain impact erosivity depends on the surface-normal component of kinetic impact energy, independent of the actual medium through which the grain moves (e.g., air or water), it scales inversely with bedrock substrate tensile strength, σ_{rock} (Beer and Lamb, 2021; Scheingross et al., 2014). Thus, dry grain impact abrasion, $V_{cell} = k_{ero}\ \varepsilon_{kin,n}$, can be transformed to fit into the bedrock erodibility framework established for fluvial abrasion and grain drop experiments on rocks of different strengths, $V_{rock} = c_{ero}\frac{\varepsilon_{kin,n}}{\sigma_{rock}^2}$ (with a bedrock erodibility conversion factor of $c_{ero} = 3.8 \times 10^4$ J/Pa^2; Beer and Lamb, 2021). Conversely, any massive bedrock as defined by its tensile strength can be applied within DGAM by multiplying grain impact erosivity (Equation 12). Compared to our used foam substrate, V_{rock} would shift to one order of magnitude higher abrasion rates for a weak sandstone ($\sigma_{rock} = 0.1\mathrm{MPa}$) or to four orders of magnitude lower abrasion rates for quartzite ($\sigma_{rock} = 20\mathrm{MPa}$; cf. the measured rock tensile strengths in Sklar and Dietrich, 2001).

There may be additional important tradeoffs between the erodibility of bedrock and the frequency and magnitude of rockfall events. For example, bedrock tends to be stronger in massive rock with low fracture density, like granite (cf. Figure 1E), which should slow rockfall erosion rates by reducing k_{ero}. In addition, granite also tends to weather into small grains, which would have low kinetic energy and therefore could reduce rockfall erosion rates further (Equation 9). In contrast, jointed rocks like sandstone or columnar basalt produce more intact rock blocks (cf. Figure 1A and B; Ward et al., 2011). Due to the more-than-linear dependence of abrasion on impactor size (Figure 9B, lower panels), fewer more massive rocks would produce more erosion than more frequent events with smaller rocks. These ideas could be incorporated in a future effort to describe the rockfall generation process, which is needed to drive the rockfall abrasion model.

5.4. Rockfall erosion on low gradients

Our experiments and modelling confirm that bedrock hillslopes can be eroded by dry rockfall abrasion even below the angle of repose (Figure 3; DiBiase et al., 2017; Pelletier et al., 2008; Sun et al., 2021). Given energetic rockfall and low friction angles relative to the surface roughness (DiBiase et al., 2017), even small grain sizes are able to traverse rocky slopes (Figure 9B). As their impact energy is not diffused into granular debris like on granular substrate (Figure 1G), it contributes to rock fracturing and subsequent abrasion (Figure 1H). Thus, dry rockfall, as an endmember of dry granular avalanching (Howard, 1998), is an erosive process not restricted to steep alpine environments.

The abundance of rockfall on rocky slopes in both dry and humid areas permit to elucidate the absolute and relative contribution of rockfall-driven erosion to earthen and planetary surface evolution, so far generally ascribed to fluvial or aeolian erosion (e.g., Figure 1A to D). While in steeper areas rockfall may outpace other erosive processes and create indicative topographic features (cf. Howard and Selby, 2009), at the foot slopes of lower gradient, dry bedrock abrasion could set preferential routes for fluvial mass transport processes and this way enhance their channelization.

5.5. Formation of rocky chutes

As shown, rockfall-prone hillslopes evolve into bumpy and channelized chute topography (Figure 3 and Figure 4A and D; Blackwelder, 1942), which steers grains into preferential pathways resulting in topographic feedback (Figure 4B and C; cf. Sun et al., 2021). This transient process was successfully reproduced by the dry grain abrasion model DGAM fitted with a fixed impact shock term coefficient, $\kappa_{shock} = 0.8$ m^{-1} (Figure 10 and Figure S3). Improvement of this calibration could have been reached by better constraining the initial grain entrance conditions, though we took the approach of modeling the inlet conditions as random. The experimentally observed and modeled topographies generally resemble earthen and planetary rocky hillslope topography (Blackwelder, 1942), showing bedrock chutes and gully alcoves with downslope bumps and channels (Figure 3 and Figure 10 vs. Figure 1A to D). The lateral grain mobility (so far treated by probabilistic direction-sampling in DGAM, Table S1) was not retrievable from the vertical PIV camera in our experiments. Grain spread transience would help quantify the topographic steering feedback and its separation from diffusional processes (Jop et al., 2005; Williams and Furbish, 2021).

As long as rocky hillslopes remain free of cover (from regolith, saprolite, or vegetation), continuous and local dry grain abrasion will create rills that fuel a sequence of downhill-wandering troughs and rims (Figure 3B and 10A, B; Sun et al., 2021; cf. examples in Figure 1F and H), somehow an antipode to upstream-migrating knickpoints in (bedrock) rivers driven by fluvial sediment transport (Berlin and Anderson, 2007; Crosby and Whipple, 2006; DiBiase et al., 2015; Grimaud et al., 2016). Grain routing around sediment patches (Figures 1A and 3B) and grain deflection from elevated topography will enhance downhill channelization, which over time can lead to chutes (Figure 3A right panel, Figure 4C) or even gully channels (Figure 1D) by a self-enhancing process. Model-predicted topographies resembled both throughs (Figure 10A vs. Figure 3A right panel) and parallel rills (Figure 10B vs. Figure 3A central panel). The physical steering process of grains around resting sediment patches, as in the troughs of the experiments (Figure 3B), has not implicitly been implemented in the DGA model so far, and would require parameterizations of grain-grain interaction, grain piling (with varying angle of repose), and release mechanisms.

Talus cover from lower-sloping regions downhill reaching up onto the active abrasion area will suddenly terminate the process and seal the rocky surface due to rockfall grains starting to rest below their angle of repose, i.e., shielding a so-called sub-debris or Richter denudation slope below (a rectilinear, $35.0°$ thinly-covered rocky hillslope; Rapp, 1960). Termination will happen given short hillslope lengths, large amounts of simultaneous rockfall grains (i.e. dry grain avalanches), or low talus removal rates by other processes. Thus, there is potential that large talus cones or ramparts actually cover and hide channelized rocky slopes initially created by dry rockfall abrasion – a topic that could be verified by studying impact crater degeneration or escarpment retreat in dry planetary areas (Golombek et al., 2014; Ward et al., 2011).

5.5. Application to other planets

Dry grain abrasion modeling can generally be performed for any planetary body by adjusting gravitational acceleration. Though, there likely is no significant influence of this parameter on model mode II (grain rolling and sliding; not studied here; cf. Atwood-Stone and

McEwen, 2013), as there also is none on mode I (grain hopping) besides the influence on the acceleration of the grains during hopping. Air (or other gas) drag during the grain trajectories is neglected in the model since we deal with relatively low velocities and small, compact grains. Specifically, dry grain abrasion could be modeled in concert with other erosion processes (such as diffusion) to study the degradation of planetary crater walls, etc. (Golombek et al., 2014). This will help verify if dry bedrock abrasion is a reason why crater walls remain rocky or how low-sloping sinuous gully channels are maintained over time (Mangold et al., 2010).

Dry grain abrasion modeling on planetary surfaces is feasible considering rock or ice-cemented sediments using estimates of the substrate's tensile strengths (Beer et al., 2019). For example, low-fractured basaltic rock on Mars may have a tensile strength of σ_{rock}~10 MPa, which certainly is much lower at fractured impact craters (Wright et al., 2022; Figure 1D). Ice-cemented sediment near the melting point has tensile strengths similar to our applied foam ($\sigma_{foam} = 0.1$MPa), whereas colder permafrost can have tensile strengths again similar to basalt (Akagawa and Nishisato, 2009; Azmatch et al., 2010; Yuanlin and Carbee, 1987). Given dry regions on Earth, absolute dryness on the Moon, and current dry conditions on Mars (Figure 1A to D), together with abundant rocky hillslope areas and rockfall activity (Bickel et al., 2020a, 2020b; Dickson and Head, 2009; Kumar et al., 2013; Vijayan et al., 2022; Xiao et al., 2013), the rockfall abrasion process has potential to be a local to regional sculptor of planetary hillslopes. Shattered rocky crater walls and caprock-topped badlands are ideal sites for the process to occur. The spatio-temporal imprint of dry rockfall abrasion, specifically its distinction from and interaction with fluvial processes (Figure 1G vs. H; Levin et al., 2022), remains to be studied in detail, both for Earth and planetary hillslopes.

5 Conclusions

Our experiments and modeling show that bedrock abrasion by dry, impacting rockfall can erode and in some cases channelize rocky hillslopes. The model captures the trends in the experiments to first order by including the physics of ballistic trajectories and a bedrock wear (abrasion) relation that depends on the surface-normal kinetic energy of the impactor. Erosive grains can hop on slopes even shallower than the angle of repose (at least down to $\mathbf{20}$°), and thus contribute to landscape evolution in areas where fluvial and debris flow processes are thought to dominate. We found that increasing rockfall grain size has the most substantial effect to increase abrasion amounts due to a nonlinear relationship. Increasing hillslope gradient also caused faster erosion rates.

Hopping grains are routed around topographic highs, which steer grains trajectories in a self-enhancing feedback. First, a bumpy surface evolves with patches of immobile sediment collecting in lows (troughs) due to greater friction angles of grain piles. Around these piles and bedrock highs, shallow rills form, which coalesce into chutes and finally into emerging channels further downslope. These channels increasingly attract subsequent grains, focusing abrasion into their centers, and cause a sequence of troughs wandering downslope. The rockfall abrasion

process will terminate abruptly, where talus grows uphill from the toe of the hillslope or by coalescence of local resting sediment patches.

Given abundant rocky hillslopes and rockfall sources from cliffs and outcrops (Blackwelder, 1942; Howard and Selby, 2009; Ward et al., 2011), dry impact-driven bedrock abrasion is a conceivable contributor to Earth and planetary hillslope evolution. It could be important in high mountain rockfall areas, dry climate scarpland retreat, and in planetary surface crater decay. The model explicitly includes gravity and can be scaled to other planets.

Acknowledgments, Samples, and Data

We are thankful to Joel Scheingross for help with PU foam selection, to Roman DiBiase for providing his model code, and to Kim Miller for measuring grain friction angles. Thorough comments from three anonymous reviewers and the associate editor Kathy Barnhart greatly helped to improve the manuscript. This study was supported by SNSF grant P2EZP2_172109 to ARB, Caltech SURF fellowships to JNF and ZM, China Scholarship Council grant 201906410043 and NSFC Grant 42202120 to ZS, and NASA grant 80NSSC19K1269 and NSF grant 1558479 to MPL.

Data Accessibility

The experimental data and the dry gravel abrasion model DGAM code (in R language) will be made publicly avaliable at https://data.caltech.edu or at https://fdat.uni-tuebingen.de/.

Notation

a_{grav}	acceleration due to gravity [m/s^2]
c_{ero}	bedrock erodibility conversion factor [J/P^2]
d_{cell}	model cell size [m]
d_{grain}	rockfall grain diameter [m]
h_{hop}	grain hop height (trajectory maximum above crossed cell boundaries) [m]
k_{ero}	bedrock erosion factor (grain erosivity) [m^3/J or ms^2/kg]
l_{flume}	length of the laboratory flume [m]
l_{hop}	grain hop length [m]
$l_{hop,0}$	grain hop length at entrance of a grain into the model domain [m]
m_{grain}	rockfall grain mass [kg]
$m_{grains,tot}$	total mass of all grains in one experiment [kg]
n_{cells}	number of DEM cells traversed by a grain's trajectory [-]
$n_{grains,tot}$	total number of grains used in an experiment [-]
$n_{imps,tot}$	total number of grain impacts per grain down the laboratory flume [-]
t_{hop}	grain hop time [s]
V_{flume}	total volumetric foam abrasion of an experiment from grain impacts [m^3]
V_{cell}	volumetric abrasion of a cell by a grain impact [m^3]
V_{rock}	volumetric abrasion of a bedrock cell by a grain impact [m^3]
v_{in}	grain impact velocity [m/s]
$v_{in,0}$	grain impact velocity at entrance of a grain into the model domain [m/s]

$v_{in,n}$	surface-normal component of the grain impact velocity [m/s]
v_{out}	grain deflection velocity [m/s]
$v_{out,0}$	grain deflection velocity before entrance of a grain into the model domain [m/s]
w_{cell}	vertical cell abrasion or wear [m]
X, Y, Z	cell coordinate (X: downflume, Y: lateral, Z: vertical) [-]
$Z_{boundary}$	surface height at the boundary between two DEM cells [m]
Z_{traj}	grain trajectory height above a cell boundary [m]
α_{in}	absolute grain impact angle [°]
$\alpha_{in,0}$	absolute grain impact angle at entrance of a grain into the model domain [°]
α_{out}	absolute grain deflection angle [°]
$\alpha_{out,0}$	absolute grain deflection angle at entrance of a grain into model domain [°]
ε_{kin}	grain kinetic impact energy [J]
$\varepsilon_{kin,n}$	surface-normal component of the grain kinetic impact energy [J]
Δt	grain impact time [s]
ΔXY	horizontal distance between two cells [m]
ΔZ	vertical distance between two cells [m]
ξ	grain hop direction in D8 [-]
κ_{shock}	impact shock term [1/m]
σ_{foam}	tensile strength of the polyurethane foam [MPa]
σ_{rock}	tensile strength of bedrock [MPa]
θ_{cell}	cell slope angle [°]
θ_{slope}	hillslope angle or flume slope angle [°]
Φ_{surf}	dynamic friction angle between grain and (bedrock) surface [°]
Φ_{pocket}	grain pocket friction angle [°]
μ_{eff}	effective grain friction angle [°]

References

Akagawa, S., Nishisato, K., 2009. Tensile strength of frozen soil in the temperature range of the frozen fringe. Cold Reg. Sci. Technol. 57, 13–22. https://doi.org/10.1016/j.coldregions.2009.01.002

André, M.-F., 1997. Holocene Rockwall Retreat in Svalbard: A Triple-Rate Evolution. Earth Surf. Process. Landf. 22, 423–440.

Atwood-Stone, C., McEwen, A.S., 2013. Avalanche slope angles in low-gravity environments from active Martian sand dunes. Geophys. Res. Lett. 40, 2929–2934. https://doi.org/10.1002/grl.50586

Azmatch, T.F., Sego, D.C., Arenson, L.U., Biggar, K.W., 2010. Tensile Strength of Frozen Soils Using Four-Point Bending Test 8.

Beer, A.R., Lamb, M.P., 2021. Abrasion regimes in fluvial bedrock incision. Geology 49, 682–686. https://doi.org/10.1130/G48466.1

Beer, A.R., Lamb, M.P., Ulizio, T.P., Ma, Z., Hughes, M.N., Fraeman, A.A., Arvidson, R.E., Golombek, M.P., Dickson, J.L., 2019. Bedrock gully formatiom by dry rockfall, in: LPI Contrib. Presented at the Ninth International Conference on Mars 2019.

Beer, A.R., Turowski, J.M., 2021. From process to centuries: Upscaling field-calibrated models of fluvial bedrock erosion. Geophys. Res. Lett. https://doi.org/10.1029/2021GL093415

Benjamin, J., Rosser, N.J., Brain, M.J., 2020. Emergent characteristics of rockfall inventories captured at a regional scale. Earth Surf. Process. Landf. 45, 2773–2787. https://doi.org/10.1002/esp.4929

Berlin, M.M., Anderson, R.S., 2007. Modeling of knickpoint retreat on the Roan Plateau, western Colorado. J. Geophys. Res. 112, F03S06. https://doi.org/10.1029/2006JF000553

Bickel, V.T., Aaron, J., Manconi, A., Loew, S., Mall, U., 2020a. Impacts drive lunar rockfalls over billions of years. Nat. Commun. 11, 2862. https://doi.org/10.1038/s41467-020-16653-3

Bickel, V.T., Conway, S.J., Tesson, P.-A., Manconi, A., Loew, S., Mall, U., 2020b. Deep Learning-Driven Detection and Mapping of Rockfalls on Mars. IEEE J. Sel. Top. Appl. Earth Obs. Remote Sens. 13, 2831–2841. https://doi.org/10.1109/JSTARS.2020.2991588

Blackwelder, E., 1942. The process of mountain sculpture by rolling debris. J. Geomorphol. 4, 324–328.

Brian Dade, W., Huppert, H.E., 1998. Long-runout rockfalls. Geology 26, 803. https://doi.org/10.1130/0091-7613(1998)026<0803:LRR>2.3.CO;2

CloudCompare, 2022. CloudCompare (version 2.12) [GPL software].

Collins, B.D., Stock, G.M., 2016. Rockfall triggering by cyclic thermal stressing of exfoliation fractures. Nat. Geosci. 9, 395–400. https://doi.org/10.1038/ngeo2686

Conway, S.J., Balme, M.R., Kreslavsky, M.A., Murray, J.B., Towner, M.C., 2015. The comparison of topographic long profiles of gullies on Earth to gullies on Mars: A signal of water on Mars. Icarus 253, 189–204. https://doi.org/10.1016/j.icarus.2015.03.009

Crosby, B.T., Whipple, K.X., 2006. Knickpoint initiation and distribution within fluvial networks: 236 waterfalls in the Waipaoa River, North Island, New Zealand. Geomorphology 82, 16–38. https://doi.org/10.1016/j.geomorph.2005.08.023

D'Amato, J., Hantz, D., Guerin, A., Jaboyedoff, M., Baillet, L., Mariscal, A., 2016. Influence of meteorological factors on rockfall occurrence in a middle mountain limestone cliff. Nat. Hazards Earth Syst. Sci. 16, 719–735. https://doi.org/10.5194/nhess-16-719-2016

Delannay, R., Valance, A., Mangeney, A., Roche, O., Richard, P., 2017. Granular and particle-laden flows: from laboratory experiments to field observations. J. Phys. Appl. Phys. 50, 053001. https://doi.org/10.1088/1361-6463/50/5/053001

DiBiase, R.A., Lamb, M.P., Ganti, V., Booth, A.M., 2017. Slope, grain size, and roughness controls on dry sediment transport and storage on steep hillslopes. J. Geophys. Res. Earth Surf. 122, 941–960. https://doi.org/10.1002/2016JF003970

DiBiase, R.A., Whipple, K.X., Lamb, M.P., Heimsath, A.M., 2015. The role of waterfalls and knickzones in controlling the style and pace of landscape adjustment in the western San Gabriel Mountains, California. Geol. Soc. Am. Bull. 127, 539–559. https://doi.org/10.1130/B31113.1

Dickson, J.L., Head, J.W., 2009. The formation and evolution of youthful gullies on Mars: Gullies as the late-stage phase of Mars' most recent ice age. Icarus 204, 63–86. https://doi.org/10.1016/j.icarus.2009.06.018

Dickson, J.L., Head, J.W., Kreslavsky, M., 2007. Martian gullies in the southern mid-latitudes of Mars: Evidence for climate-controlled formation of young fluvial features based upon local and global topography. Icarus 188, 315–323. https://doi.org/10.1016/j.icarus.2006.11.020

Dorren, L.K.A., Maier, B., Putters, U.S., Seijmonsbergen, A.C., 2004. Combining field and modelling techniques to assess rockfall dynamics on a protection forest hillslope in the European Alps. Geomorphology 57, 151–167. https://doi.org/10.1016/S0169-555X(03)00100-4

Engel, P.A., 1978. Impact Wear of Materials. Elsevier.

Frayssines, M., Hantz, D., 2006. Failure mechanisms and triggering factors in calcareous cliffs of the Subalpine Ranges (French Alps). Eng. Geol. 86, 256–270. https://doi.org/10.1016/j.enggeo.2006.05.009

Gabet, E.J., Mendoza, M.K., 2012. Particle transport over rough hillslope surfaces by dry ravel: Experiments and simulations with implications for nonlocal sediment flux: PARTICLE TRANSPORT OVER ROUGH SURFACES. J. Geophys. Res. Earth Surf. 117, n/a-n/a. https://doi.org/10.1029/2011JF002229

Golombek, M.P., Warner, N.H., Ganti, V., Lamb, M.P., Parker, T.J., Fergason, R.L., Sullivan, R., 2014. Small crater modification on Meridiani Planum and implications for erosion rates and climate change on Mars: Small Crater Modification on Mars. J. Geophys. Res. Planets 119, 2522–2547. https://doi.org/10.1002/2014JE004658

Grenon, M., Hadjigeorgiou, J., 2008. A design methodology for rock slopes susceptible to wedge failure using fracture system modelling. Eng. Geol. 96, 78–93. https://doi.org/10.1016/j.enggeo.2007.10.002

Grimaud, J.-L., Paola, C., Voller, V., 2016. Experimental migration of knickpoints: influence of style of base-level fall and bed lithology. Earth Surf. Dyn. 4, 11–23. https://doi.org/10.5194/esurf-4-11-2016

Guerin, A., Rossetti, J.-P., Hantz, D., Jaboyedoff, M., 2013. Estimating rock fall frequency in a limestone cliff using LIDAR measurements 9.

Hales, T.C., Roering, J.J., 2007. Climatic controls on frost cracking and implications for the evolution of bedrock landscapes. J. Geophys. Res. 112, F02033. https://doi.org/10.1029/2006JF000616

Heldmann, J.L., Mellon, M.T., 2004. Observations of martian gullies and constraints on potential formation mechanisms. Icarus 168, 285–304. https://doi.org/10.1016/j.icarus.2003.11.024

Howard, A.D., 2007. Simulating the development of Martian highland landscapes through the interaction of impact cratering, fluvial erosion, and variable hydrologic forcing. Geomorphology 91, 332–363. https://doi.org/10.1016/j.geomorph.2007.04.017

Howard, A.D., 1998. Long profile development of bedrock channels, in: Tinkler, J., Wohl, E. (Eds.), Geophysical Monograph Series. American Geophysical Union, Washington, D. C., pp. 297–319. https://doi.org/10.1029/GM107p0153

Howard, A.D., Selby, M.J., 2009. Rock slopes, in: Parsons, A.J., Abrahams, A.D. (Eds.), Geomorphology of Desert Environments. Springer Netherlands, Dordrecht. https://doi.org/10.1007/978-1-4020-5719-9

Jop, P., Forterre, Y., Pouliquen, O., 2005. Crucial role of sidewalls in granular surface flows: consequences for the rheology. J. Fluid Mech. 541, 167. https://doi.org/10.1017/S0022112005005987

Kirkby, M.J., Statham, I., 1975. Surface Stone Movement and Scree Formation. J. Geol. 83, 349–362.

Kokelaar, B.P., Bahia, R.S., Joy, K.H., Viroulet, S., Gray, J.M.N.T., 2017. Granular avalanches on the Moon: Mass-wasting conditions, processes, and features: Granular Avalanches on the Moon. J. Geophys. Res. Planets 122, 1893–1925. https://doi.org/10.1002/2017JE005320

Kumar, S.P., Keerthi, V., Senthil Kumar, A., Mustard, J., Gopala Krishna, B., Amitabh, Ostrach, L.R., Kring, David.A., Kiran Kumar, A.S., Goswami, J.N., 2013. Gullies and landslides on the Moon: Evidence for dry-granular flows: GULLIES AND LANDSLIDES ON THE MOON. J. Geophys. Res. Planets 118, 206–223. https://doi.org/10.1002/jgre.20043

Lague, D., Brodu, N., Leroux, J., 2013. Accurate 3D comparison of complex topography with terrestrial laser scanner: Application to the Rangitikei canyon (N-Z). ISPRS J. Photogramm. Remote Sens. 82, 10–26. https://doi.org/10.1016/j.isprsjprs.2013.04.009

Lajeunesse, E., Mangeney-Castelnau, A., Vilotte, J.P., 2004. Spreading of a granular mass on a horizontal plane. Phys. Fluids 16, 2371–2381. https://doi.org/10.1063/1.1736611

Lamb, M.P., Finnegan, N.J., Scheingross, J.S., Sklar, L.S., 2015. New insights into the mechanics of fluvial bedrock erosion through flume experiments and theory. Geomorphology 244, 33–55. https://doi.org/10.1016/j.geomorph.2015.03.003

Le Roy, G., Helmstetter, A., Amitrano, D., Guyoton, F., Le Roux-Mallouf, R., 2019. Seismic Analysis of the Detachment and Impact Phases of a Rockfall and Application for Estimating Rockfall Volume and Free-Fall Height. J. Geophys. Res. Earth Surf. 124, 2602–2622. https://doi.org/10.1029/2019JF004999

Leith, K., Moore, J.R., Amann, F., Loew, S., 2014. In situ stress control on microcrack generation and macroscopic extensional fracture in exhuming bedrock. J. Geophys. Res. Solid Earth 119, 594–615. https://doi.org/10.1002/2012JB009801

Levin, J.N., Dickson, J.L., Lamb, M.P., 2022. Evaluating the role of volatiles in bedrock chute formation on the Moon and Mars. Icarus 373, 114774. https://doi.org/10.1016/j.icarus.2021.114774

Loye, A., Pedrazzini, A., Theule, J.I., Jaboyedoff, M., Liébault, F., Metzger, R., 2012. Influence of bedrock structures on the spatial pattern of erosional landforms in small alpine catchments. Earth Surf. Process. Landf. 37, 1407–1423. https://doi.org/10.1002/esp.3285

Mackey, B.H., Quigley, M.C., 2014. Strong proximal earthquakes revealed by cosmogenic 3He dating of prehistoric rockfalls, Christchurch, New Zealand. Geology 42, 975–978. https://doi.org/10.1130/G36149.1

Mangold, N., Mangeney, A., Migeon, V., Ansan, V., Lucas, A., Baratoux, D., Bouchut, F., 2010. Sinuous gullies on Mars: Frequency, distribution, and implications for flow properties. J. Geophys. Res. 115, E11001. https://doi.org/10.1029/2009JE003540

Matasci, B., Stock, G.M., Jaboyedoff, M., Carrea, D., Collins, B.D., Guérin, A., Matasci, G., Ravanel, L., 2018. Assessing rockfall susceptibility in steep and overhanging slopes using three-dimensional analysis of failure mechanisms. Landslides 15, 859–878. https://doi.org/10.1007/s10346-017-0911-y

McDonald, R.R., Anderson, R.S., 1996. Constraints on Eolian Grain Flow Dynamics Through Laboratory Experiments on Sand Slopes. SEPM J. Sediment. Res. Vol. 66. https://doi.org/10.1306/D42683D3-2B26-11D7-8648000102C1865D

Mergili, M., Jaboyedoff, M., Pullarello, J., Pudasaini, S.P., 2020. Back calculation of the 2017 Piz Cengalo–Bondo landslide cascade with r.avaflow: what we can do and what we can learn. Nat. Hazards Earth Syst. Sci. 20, 505–520. https://doi.org/10.5194/nhess-20-505-2020

Messenzehl, K., Meyer, H., Otto, J.-C., Hoffmann, T., Dikau, R., 2017. Regional-scale controls on the spatial activity of rockfalls (Turtmann Valley, Swiss Alps) — A multivariate modeling approach. Geomorphology 287, 29–45. https://doi.org/10.1016/j.geomorph.2016.01.008

Mokudai K., Ikeda H., Iijima H., Yuhora K., 2011. Experimental Study of Bedrock Erosion by Rock Fall. Geogr. Stud. 86, 108–114. https://doi.org/10.7886/hgs.86.108

Montgomery, D.R., Dietrich, W.E., 1994. A physically based model for the topographic control on shallow landsliding. Water Resour. Res. 30, 1153–1171. https://doi.org/10.1029/93WR02979

Moore, J.R., Sanders, J.W., Dietrich, W.E., Glaser, S.D., 2009. Influence of rock mass strength on the erosion rate of alpine cliffs. Earth Surf. Process. Landf. 34, 1339–1352. https://doi.org/10.1002/esp.1821

Neely, A.B., DiBiase, R.A., 2020. Drainage Area, Bedrock Fracture Spacing, and Weathering Controls on Landscape-Scale Patterns in Surface Sediment Grain Size. J. Geophys. Res. Earth Surf. 125. https://doi.org/10.1029/2020JF005560

Neilson, J.H., Gilchrist, A., 1968. Erosion by a stream of solid particles. Wear 11, 111–122. https://doi.org/10.1016/0043-1648(68)90591-7

Pelletier, J.D., Kolb, K.J., McEwen, A.S., Kirk, R.L., 2008. Recent bright gully deposits on Mars: Wet or dry flow? Geology 36, 211. https://doi.org/10.1130/G24346A.1

Prancevic, J.P., Lamb, M.P., 2015. Particle friction angles in steep mountain channels: Friction angles in mountain channels. J. Geophys. Res. Earth Surf. 120, 242–259. https://doi.org/10.1002/2014JF003286

Python, 2021. Python packages OpenCV and TrackPy.

Quartier, L., Andreotti, B., Douady, S., Daerr, A., 2000. Dynamics of a grain on a sandpile model. Phys. Rev. E 62, 8299–8307. https://doi.org/10.1103/PhysRevE.62.8299

Rapp, A., 1960. Talus slopes and mountain walls at Tempelfjorden, Spitsbergen (No. 96), Norsl Polarinstitut Skrifter. University of Oslo, Oslo.

Sass, O., Krautblatter, M., 2007. Debris flow-dominated and rockfall-dominated talus slopes: Genetic models derived from GPR measurements. Geomorphology 86, 176–192. https://doi.org/10.1016/j.geomorph.2006.08.012

Scheingross, J.S., Brun, F., Lo, D.Y., Omerdin, K., Lamb, M.P., 2014. Experimental evidence for fluvial bedrock incision by suspended and bedload sediment. Geology 42, 523–526. https://doi.org/10.1130/G35432.1

Selby, M.J., 1982. Hillslope Materials and Processes. Oxford University Press, Oxford, UK.

Shinbrot, T., Duong, N.-H., Kwan, L., Alvarez, M.M., 2004. Dry granular flows can generate surface features resembling those seen in Martian gullies. Proc. Natl. Acad. Sci. 101, 8542–8546. https://doi.org/10.1073/pnas.0308251101

Shugar, D.H., Jacquemart, M., Shean, D., Bhushan, S., Upadhyay, K., Sattar, A., Schwanghart, W., McBride, S., de Vries, M.V.W., Mergili, M., Emmer, A., Deschamps-Berger, C., McDonnell, M., Bhambri, R., Allen, S., Berthier, E., Carrivick, J.L., Clague, J.J., Dokukin, M., Dunning, S.A., Frey, H., Gascoin, S., Haritashya, U.K., Huggel, C., Kääb, A., Kargel, J.S., Kavanaugh, J.L., Lacroix, P., Petley, D., Rupper, S., Azam, M.F., Cook, S.J., Dimri, A.P., Eriksson, M., Farinotti, D., Fiddes, J., Gnyawali, K.R., Harrison, S., Jha, M., Koppes, M., Kumar, A., Leinss, S., Majeed, U., Mal, S., Muhuri, A., Noetzli, J., Paul, F., Rashid, I., Sain, K., Steiner, J., Ugalde, F., Watson, C.S., Westoby, M.J., 2021. A massive rock and ice avalanche caused the 2021 disaster at Chamoli, Indian Himalaya. Science 373, 300–306. https://doi.org/10.1126/science.abh4455

Sklar, L.S., Dietrich, W.E., 2004. A mechanistic model for river incision into bedrock by saltating bed load. Water Resour. Res. 40. https://doi.org/10.1029/2003WR002496

Sklar, L.S., Dietrich, W.E., 2001. Sediment and rock strength controls on river incision into bedrock 4.

Stock, G.M., B.D., C., Santaniello, D.J., Zimmer, V.L., Wieczorek, G.F.,, Snyder, J.B., 2013. Historical Rock Falls in Yosemite National Park, California (1857–2011) (No. 746), U.S. Geological Survey Data Series.

Sun, Z., Ulizio, T.P., Fischer, J.N., Levin, J.N., Beer, A.R., Dickson, J.L., Lamb, M.P., 2021. Formation of low-gradient bedrock chutes by dry rockfall on planetary surfaces. Geology.

Turowski, J.M., Wyss, C.R., Beer, A.R., 2015. Grain size effects on energy delivery to the streambed and links to bedrock erosion. Geophys. Res. Lett. 42, 1775–1780. https://doi.org/10.1002/2015GL063159

Vijayan, S., Harish, Kimi, K.B., Tuhi, S., Vigneshwaran, K., Sinha, R.K., Conway, S.J., Sivaraman, B., Bhardwaj, A., 2022. Boulder Fall Ejecta: Present Day Activity on Mars. Geophys. Res. Lett. 49. https://doi.org/10.1029/2021GL096808

Volkwein, A., Schellenberg, K., Labiouse, V., Agliardi, F., Berger, F., Bourrier, F., Dorren, L.K.A., Gerber, W., Jaboyedoff, M., 2011. Rockfall characterisation and structural protection – a review. Nat. Hazards Earth Syst. Sci. 11, 2617–2651. https://doi.org/10.5194/nhess-11-2617-2011

Ward, D.J., Berlin, M.M., Anderson, R.S., 2011. Sediment dynamics below retreating cliffs: SEDIMENT DYNAMICS BELOW RETREATING CLIFFS. Earth Surf. Process. Landf. 36, 1023–1043. https://doi.org/10.1002/esp.2129

Wieczorek, G.F., Snyder, J.B., Alger, C.S., Isaacson, K.A., 1992. Rock falls in Yosemite Valley, California (Open-File Report 92-387), Open-File Report. National Park Service, Yosemite National Park, California.

Williams, J.G., Rosser, N.J., Hardy, R.J., Brain, M.J., 2019. The Importance of Monitoring Interval for Rockfall Magnitude-Frequency Estimation. J. Geophys. Res. Earth Surf. 124, 2841–2853. https://doi.org/10.1029/2019JF005225

938 Williams, S.G.W., Furbish, D.J., 2021. Particle energy partitioning and transverse diffusion during rarefied travel on
939 an experimental hillslope. Earth Surf. Dyn. 9, 701–721. https://doi.org/10.5194/esurf-9-701-2021
940 Wright, V., Dasent, J., Kilburn, R., Manga, M., 2022. A Minimally Cemented Shallow Crust Beneath InSight.
941 Geophys. Res. Lett. 49. https://doi.org/10.1029/2022GL099250
942 Xiao, Z., Zeng, Z., Ding, N., Molaro, J., 2013. Mass wasting features on the Moon – how active is the lunar surface?
943 Earth Planet. Sci. Lett. 376, 1–11. https://doi.org/10.1016/j.epsl.2013.06.015
944 Yuanlin, Z., Carbee, D.L., 1987. Tensile strength of frozen silt 30.

945

946 **Table 1: Outline of the dry grain abrasion experiments**, ordered by flume slope angle. Each experiment's data
947 symbol (as used in Figure 5, Figure 6, and Figure S4) refers to the relative size and shape of the used grains (large
948 vs. small, and round vs. angular). Erodible-bed experiments (*EB*) are denoted with grey background shading, and
949 fixed-bed experiments (*FB*) are of white background. More detailed measurements of the erodible bed experiments
950 *EB* are given in Table S2.
951
952 **Figure 1: Concept of rocky hillslope abrasion by dry rockfall:** Exemplary erosional rocky hillslope topography:
953 (A) plinth bedrock below a sandstone cap (Marble Canyon, AZ, USA), (B) chute channel in a basaltic lava flow
954 (Pan de Azúcar National Park, Chile), (C) basaltic bedrock gullies on Dawes crater walls on the Moon (Kumar et al.,
955 2013), and (D) furrowed Basalt bedrock gullies on Endurance Crater wall on Mars (google Mars). Exemplary sites
956 of dry grain transport over underlaying (E) granular substrate and (F) over bedrock substrate, San Gabriel
957 Mountains, CA. Conceptual sketches illustrate hillslope morphologies resulting from dry grain transport and erosion
958 over (G) gravel substrate and (H) over bedrock substrate.
959
960 **Figure 2: Dry grain abrasion model setup and experimental scheme**: (A) definitions of grain trajectory variables
961 in the dry grain abrasion model (DGAM; model scheme in Table S1; see notation section), (B) schematic of the
962 tilted flume filled with PU foam, sediment feeding and collection, terrestrial laser scanner (TLS) positions and
963 visual fields of particle imaging velocimetry (PIV), (C) picture in horizontal view on an initial smooth flume foam
964 surface, and (D) sample set of used dry, rounded rhyolite grains of d_{grain} = 0.03m.
965
966 **Figure 3: Abraded surface patterns of the erodible-bed experiments (*EB*):** (A) evolution of the foam surface
967 during *EB5* given at three temporal states, as indicated by the total grain mass run through until then ($m_{grains,tot}$).
968 Color code is for vertical surface abrasion (note different range per panel). Contours denote abrasion depths in steps
969 of grain size (d_{grain} = 1.5cm). The cleft to the bottom left in the central panel is an artifact due to missing surface
970 data. Three lateral (cross sections, cs) and one central long profile through the evolving surface of *EB5* are shown in
971 Figure 4A to C. (B) Grey-shaded surface meshes of the grain entrance area at the final experimental states, resulting
972 from different flume slope angles, grain sizes, and grain feed configurations: equal feed over the whole flume width
973 (*EB1* and *EB2*), central feed (*EB3* and *EB4*), and pointwise feed (*EB5*; cf. Table S2). Grain feed entrance directions
974 are indicated by the arrows, and flume constrictions for *EB3* and *EB4* are visible by the vertical black boards,
975 respectively. The upper flume bed section visible in (B) consisted of a fixed (non-abradable) board. Parallel blue
976 lines are horizontal (lateral) contours in 0.05m spacing, and yellow lines are vertical contours in 0.01m spacing.
977
978 **Figure 4: Transient topographic evolution of an erodible-bed experiment (*EB5*):** (A) cross sections through the
979 flume showing bed elevation below the initial surface for three experimental times and at three positions down the
980 flume (cs1=0.3m, cs2=0.65m, and cs3=1.25m; see Figure 3A left panel), (B) relative distribution of grains passing
981 through these cross sections around the three experimental times, (C) mean abrasion depth per grain impact on a
982 quadratic grain footprint (equals w_{cell} in the DGAM model), and (D) central long profile evolution down the flume
983 shown for several experimental times with indicated evolving topographic features (cf. Figure 3A right panel).
984
985 **Figure 5: Grain trajectory statistics of the experiments:** (A) a grain hop length l_{hop}, (B) grain hop height h_{hop},
986 (C) grain impact angle α_{in}, and (D) grain impact velocity v_{in} against flume slope angle Θ_{slope}. Boxplots show
987 statistics given as described in the inset in (C). Data from the erodible-bed experiments (*EB1-EB3* and *FB*5) is
988 shown with grey shading, and data from fixed-bed experiments are of white background (*FB1-FB6*). Grain shapes
989 and relative grain sizes of the experiments are indicated as symbols above (A), (cf. symbol assignments in Table 1,
990 upper part). The mean values indicated by the dotted lines ($\bar{l}_{hop}$, $\bar{h}_{hop}$, $\bar{\alpha}_{in}$, and $\bar{v}_{in}$) refer to the erodible-bed
991 experiments only, since the fixed-bed experiments likely started with higher initial grain velocities.
992
993 **Figure 6: Mean impact abrasion and grain erosivity of the erodible-bed experiments (*EB*) varying flume slope**
994 **angle**: (A) mean vertical impact abrasion, w_{cell} (i.e., abrasion volume of an impacting grain, V_{cell}, divided by cell
995 area $d_{cell}^2 = d_{grain}^2$; Equation 9), (B) abrasion volume, V_{cell}, divided by the surface-normal component of the grain's
996 impact energy, $\varepsilon_{in,n}$, called grain erosivity, k_{ero}, and (C) these values further divided by the impacting grain's cross-
997 sectional area $d_{cell}^2 = d_{grain}^2$ with two labeled values for rounded and angular grains, respectively. Relative symbol
998 size and shape are defined by used grain size and grain shape of the erodible-bed experiments (*EB*, symbols assigned
999 in Table 1, upper part). The grey-shaded area in the background denotes the common span for the angle of repose
1000 for grain piles.

Figure 7: Calibration of the DGAM model by selecting the shock term: Predicted mean grain trajectory variables divided by measured mean trajectory variables for erodible-bed experiment 2 (*EB2*), plotted against the shock term (κ_{shock}), which was varied in the modeling in steps of 0.1m^{-1}. Unity on the y-axis means ideal model-reproduction of the measurements. The selected shock term (indicated by the vertical dotted line) was chosen at the first closest general agreement.

Figure 8: Reproduction of erodible-bed experiment (*EB*) grain trajectories with DGAM: PIV-measured trajectory data and calibrated DGAM predictions along the flume for (A) grain hop length, l_{hop}, (B) grain impact velocities, v_{in}, (C) surface-normal grain impact velocity components, $v_{in,n}$, (D) grain deflection velocities, v_{out}, (E) absolute grain impact angles, α_{in}, (F) absolute grain deflection angles, α_{out}, and (G) grain impact cell abrasion volume, V_{cell}. Shown are measured PIV data for the fields of view of the three lateral PIV cameras (boxplots with median in grey, box-size of 50% interquartile range and whisker length of 1.5 times thereof, for data over 5cm bins downslope the flume) and mean DGAM predictions for 280 grains, equally sourced across the modeled flume width (black triangles). Data from erodible-bed experiment 2 (*EB2*; Table 1), PIV-camera positions are shown in Figure 2B.

Figure 9: Parameter space exploration for DGAM: Model predictions vs. experimental data for (A) varying slope angle, Θ_{slope}, and keeping grain size constant (d_{grain} = 0.03m), and (B) varying grain size, d_{grain}, and keeping slope angle constant (Θ_{slope} = 35°), respectively. Experimental PIV data is from the erodible-bed experiments (*EB*, boxplots with whiskers extending to 1.5 times the interquartile range from the box), and mean PIV data is from the fixed-bed experiments (*FB*, diamonds; Table 1). DGAM-predictions in (A) based on the erosivity-calibration for round grains (following the normalized grain erosivity 0.001m/J in Figure 6C; bold blue lines), representative for *EB3*, *EB4*, and *FB1-FB6*, while prediction for angular grains measured on another grain size is shown for comparison (normalized erosivity 0.003m/J, *EB5* and thin yellow lines). DGAM-predictions in (B) based on erosivity-calibration for angular grains, representative for *EB5* and *FB4* (bold yellow lines), while prediction for round grains measured on another slope angle is shown for comparison (*EB3* and thin blue lines). The panels per row show grain hop length, l_{hop}, grain impact velocity, v_{in}, grain impact angles, α_{in}, volumetric grain impact abrasion, V_{cell}, and local impact abrasion (i.e. V_{cell} divided by mean hop length, l_{hop}), respectively. Abrasion for the fixed-bed experiments (*FB*, diamonds) was not measured but predicted based on the erodibility of experiment *EB3*.

Figure 10: Predicted transient hillslope channelization varying rockfall grain feed: Simulations used varied grain feed patterns: (A) uniform central feed over 10 model cells, and (B) uniform feed in three inlets of 3, 4 and 3 cell widths (as indicated by the blue arrows on top of the third panels). DGAM-calibration was for erodible-bed experiment 2 (*EB5*; Table 1) with fixed $\boldsymbol{m_{grains,tot} = 800\text{tons}}$ of angular $\boldsymbol{d_{grain} = 0.20\text{m}}$ grains (normalized erosivity 0.003m/J; cf. Figure 6C) and a hillslope angle of $\boldsymbol{\Theta_{slope} = 35°}$. Shown are stacked cross-sections (cs) through the transiently abraded hillslopes in a horizontal perspective, with initial (dotted), intermediate (i.e., half-time; grey), and final topography (black), respectively (more cross-sections are given in Figure S3). The lowest panels of (A) and (B) additionally show the transient lateral distribution of passing grains down the whole slope for the three experimental times (normalized number of transported grains; bin width is 0.2m). (C) and (D) show the central long profiles (lp) for both simulations with evolving troughs and rims; the position of the cross-sections of (A) and (B) are also indicated. Modeled topographies in panels (A, B) are comparable to the experimental topographies in Figure 4A and B, long profiles in panels (C, D) are comparable to Figure 4D.

experiments			flume	dry grain properties						grain trajectory statistics†			foam abrasion	
erodible-bed	fixed-bed	symbol in Figures	slope, Θ_{slope} [°]	type	shape	surface friction angle, Φ_{surf} [°]	pocket friction angle, Φ_{pocket} [°]	size, d_{grain} [m]	total grain mass, $m_{grains,tot}$ [tons]	relative impact angle#, α_{in} [°]	impact velocity, v_{in} [m/s]	hop distance, l_{hop} [m]	total abrasion volume, V_{flume} [m^3]	grain impact erosivity, k_{ero} [cm^3/J]
*EB1**			16.7	Granite		20	34	0.061	22.5	9.5	1.1	0.16	0.090	2.65
EB2					rounded (tumbled)		34.7	0.023	8.3	9.0	1.2	0.11	0.046	1.00
EB3			19.5	Andesite		23.5	40.3	0.030	2.7	9.8	1.8	0.09	0.013	0.30
EB4									5.1	10,5^	0,8^	0,07^	0.017	1.38
EB5			35.0	Granite	angular	33.4	55.6	0.015	16.5	10.5	1.6	0.16	0.040	0.68
	FB1		20	Andesite	rounded (tumbled)	23.5	44.4	0.036	2.6e-4	6.0	1.9	0.13	-	-
	FB2		25							16.9	2.1	0.20	-	-
	FB3		30							2,7^	2,2^	0,22^	-	-
	FB4		35							19,1^	2,5^	0,32^	-	-
	FB5		40							29.8	2.4	0.23	-	-
	FB6		45							35.5	2.7	0.24	-	-

* data from Sun et al., 2021

† data from the second lateral camera (i.e. PIV-cam2, central along the flume, neither at the inlet nor at the outlet; Figure 2B)

angles are relative to the flume surface (i.e. they are not corrected for the flume slope Θ_{slope})

^ uncertain data (few measurements)

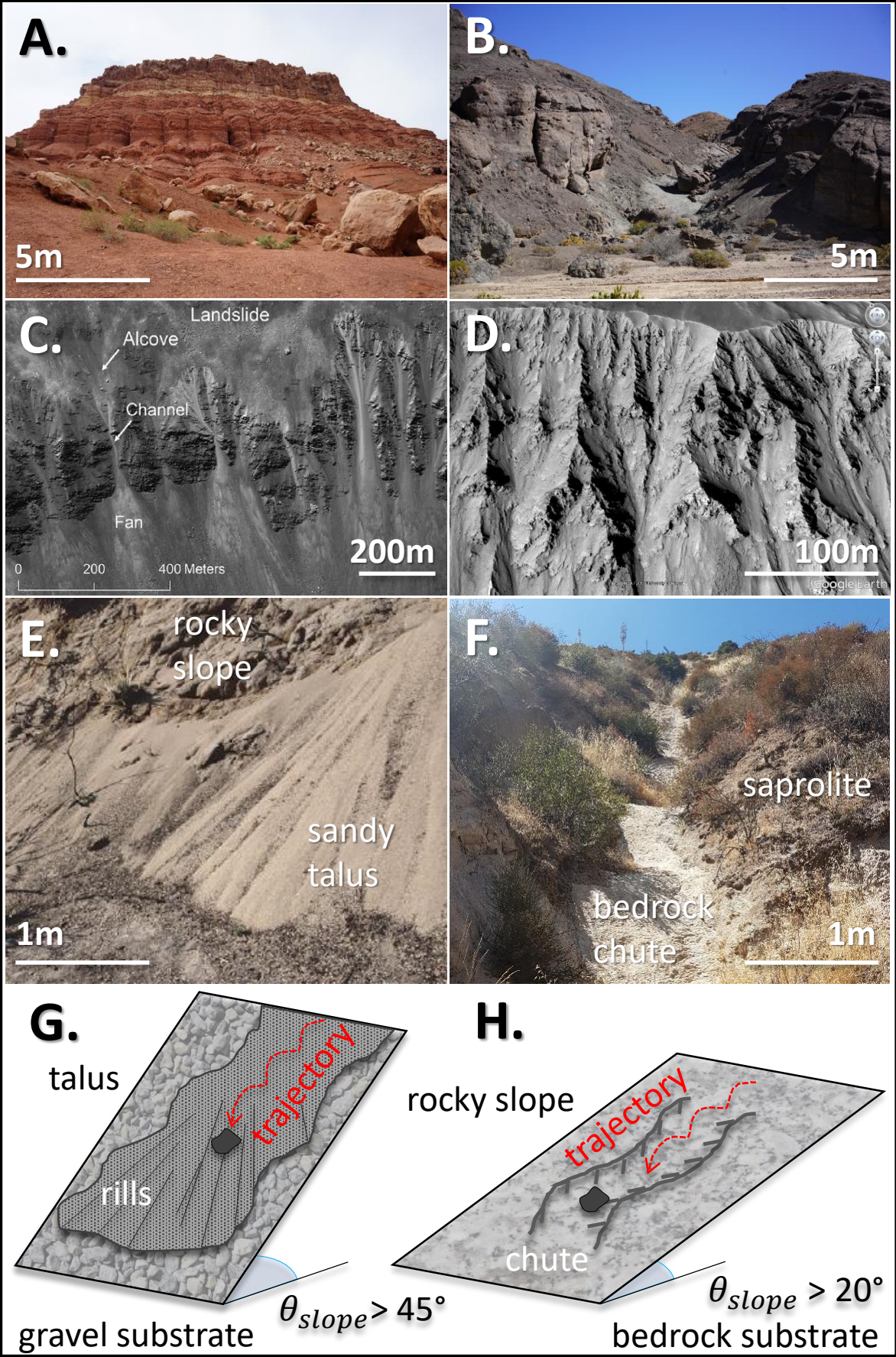
A.
5m
B.
5m
C.
Landslide
Alcove
Channel
Fan
0
200
400 Meters
200m
D.
100m
Google Earth
E.
rocky slope
sandy talus
1m
F.
saprolite
bedrock chute
1m
G.
talus
trajectory
rills
gravel substrate
$\theta_{slope} > 45°$
H.
rocky slope
trajectory
chute
$\theta_{slope} > 20°$
bedrock substrate

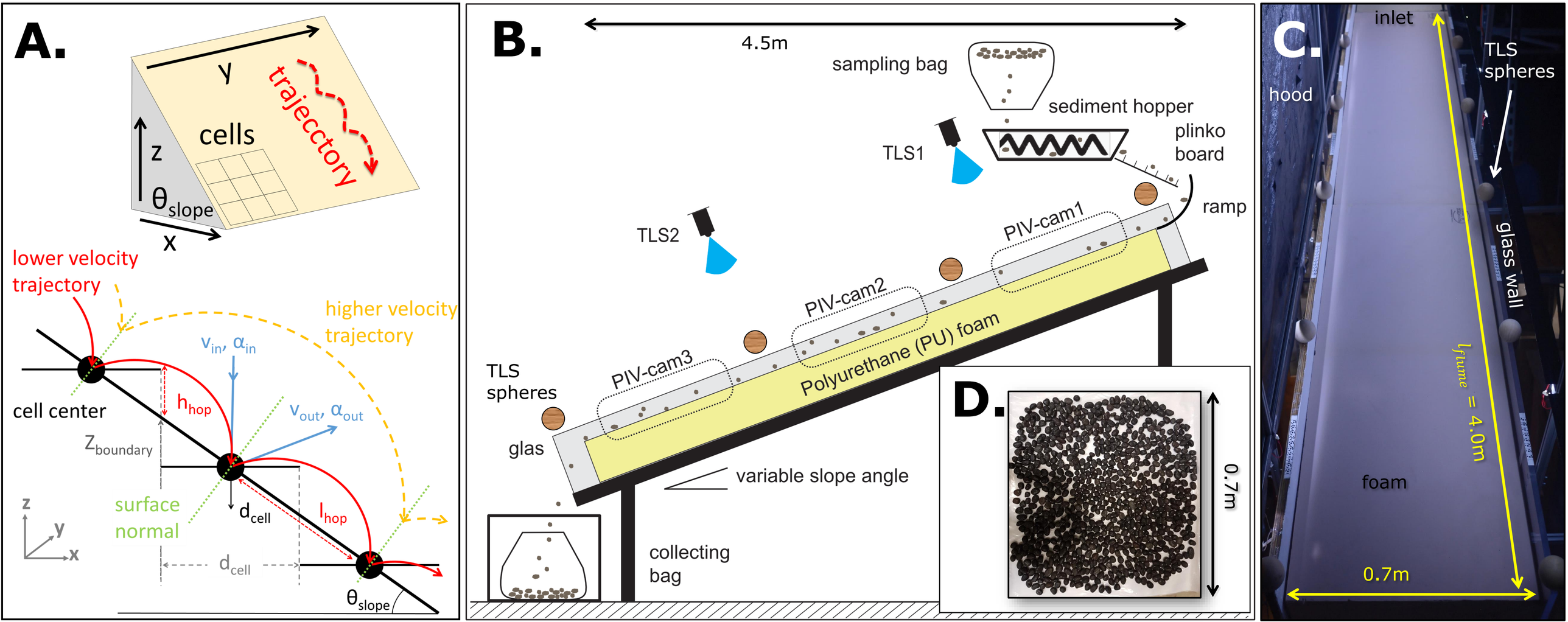
A.
y
cells
trajecctory
z
θslope
x
lower velocity trajectory
higher velocity trajectory
vin, αin
hhop
cell center
vout, αout
Zboundary
surface normal
dcell
lhop
z
y
x
dcell
θslope
B.
4.5m
sampling bag
sediment hopper
plinko board
TLS1
ramp
TLS2
PIV-cam1
PIV-cam2
PIV-cam3
TLS spheres
Polyurethane (PU) foam
glas
variable slope angle
collecting bag
D.
0.7m
C.
inlet
hood
TLS spheres
glass wall
lflume = 4.0m
foam
0.7m

A. transient topography of *EB5*

accumulated vertical abrasion [m]

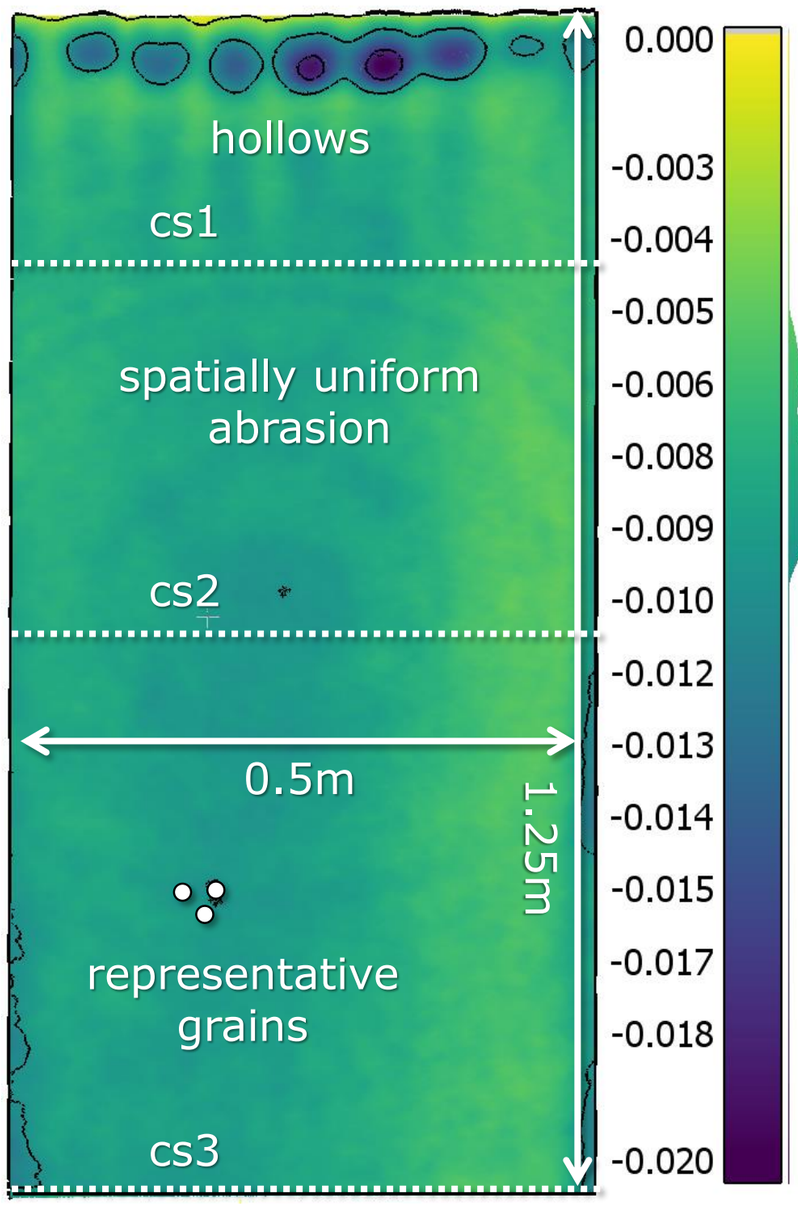

$m_{grains,tot}$ = 2.9tons

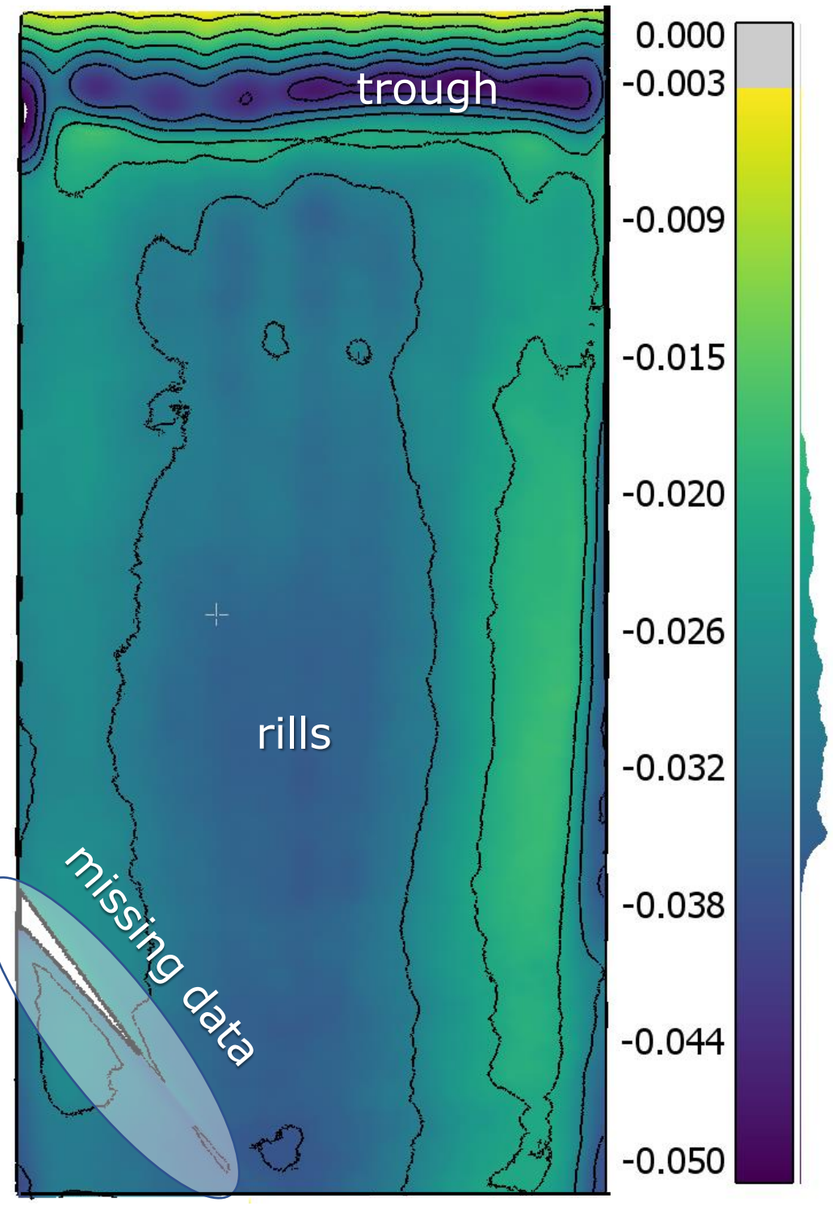

$m_{grains,tot}$ = 10.1tons

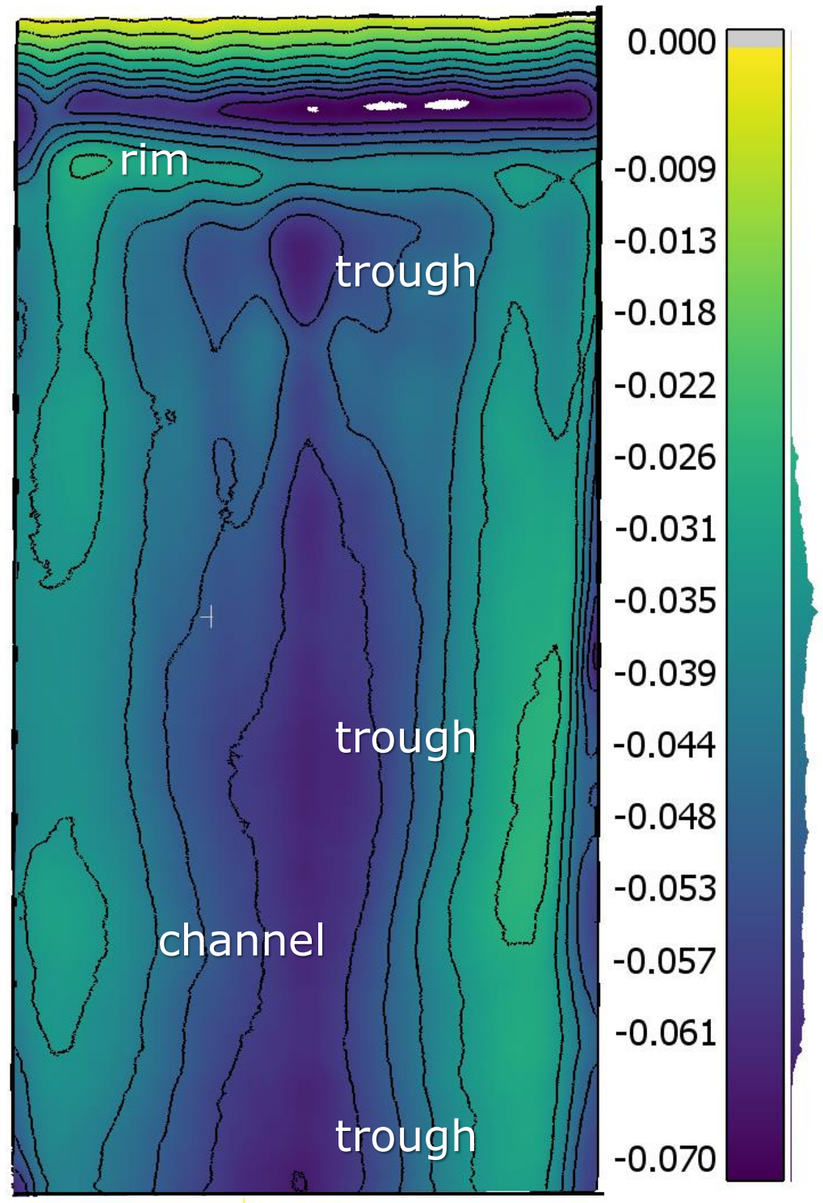

$m_{grains,tot}$ = 16.5tons

B. final erodible-bed topographies

grain feed width

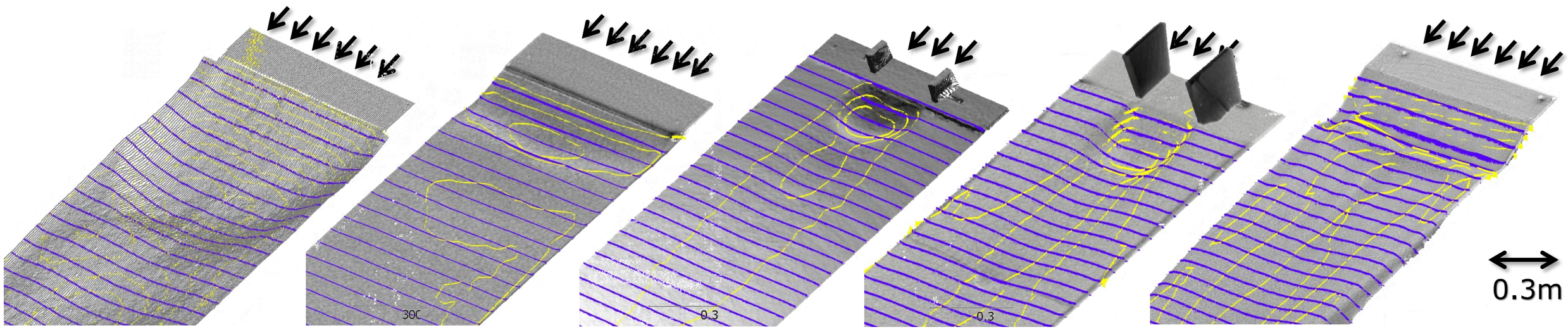

EB1	***EB2***	***EB3***	***EB4***	***EB5***
d_{grain} = 0.061m	0.023m	0.030m	0.030m	0.015m
Θ_{slope} = 16.7°	19.5°	19.5°	19.5°	35.0°

horizontal contours
vertical contours

bed elevation below initial surface [m]

0h
8h
22h
34h
cs 1
cs 2
cs 3

0
−0.05
−0.1

A.

normalized number of grains [–]

0
0.1
0.2

B.

grain impact abrasion (w_{cell}) [µm]

0
20
40

C.

0
0.3
0.6

lateral distance [m]

bed elevation b.i. surface [m]

0 h
3 h
6 h
8 h
10 h
11 h
12 h
14 h
16 h
18 h
20 h
22 h
27 h
31 h
34 h
run time

rim
rim
trough
trough
trough

0
−0.04
−0.08

0
0.25
0.5
0.75
1

distance down the flume [m]

D.

grain shape/size properties

erodible−bed
fixed−bed

hop length l_{hop} [m]

0 0.2 0.4 0.6

$\bar{l}_{hop}$

A.

experiments EB1 EB2,3; FB1 FB2 FB3 EB5,FB4 FB5 FB6

hop height h_{hop} [m]

0 0.03 0.09

$\bar{h}_{hop}$

B.

impact angle α_{in} [°]

0 40 80

95th
3rd quartile
mean
median
1st quartile
5th

$\bar{\alpha}_{in}$

θ_{slope}

C.

impact velocity v_{in} [m/s]

0 2 4

$\bar{v}_{in}$

D.

0 10 20 30 40 50

slope angle, θ_{slope} [°]

impact abrasion

w_{cell} [m]

1e−4

1e−5

1e−6

A.

span of angle of repose

erosivity

k_{ero} [m^3/J]

1e−4

1e−5

1e−6

B.

erosivity / d^2_{grain}

[m/J]

0.004

0.002

0

C.

0.003

angular grains

rounded grains

~0.001

10 20 30 40 50

slope angle, θ_{slope} [°]

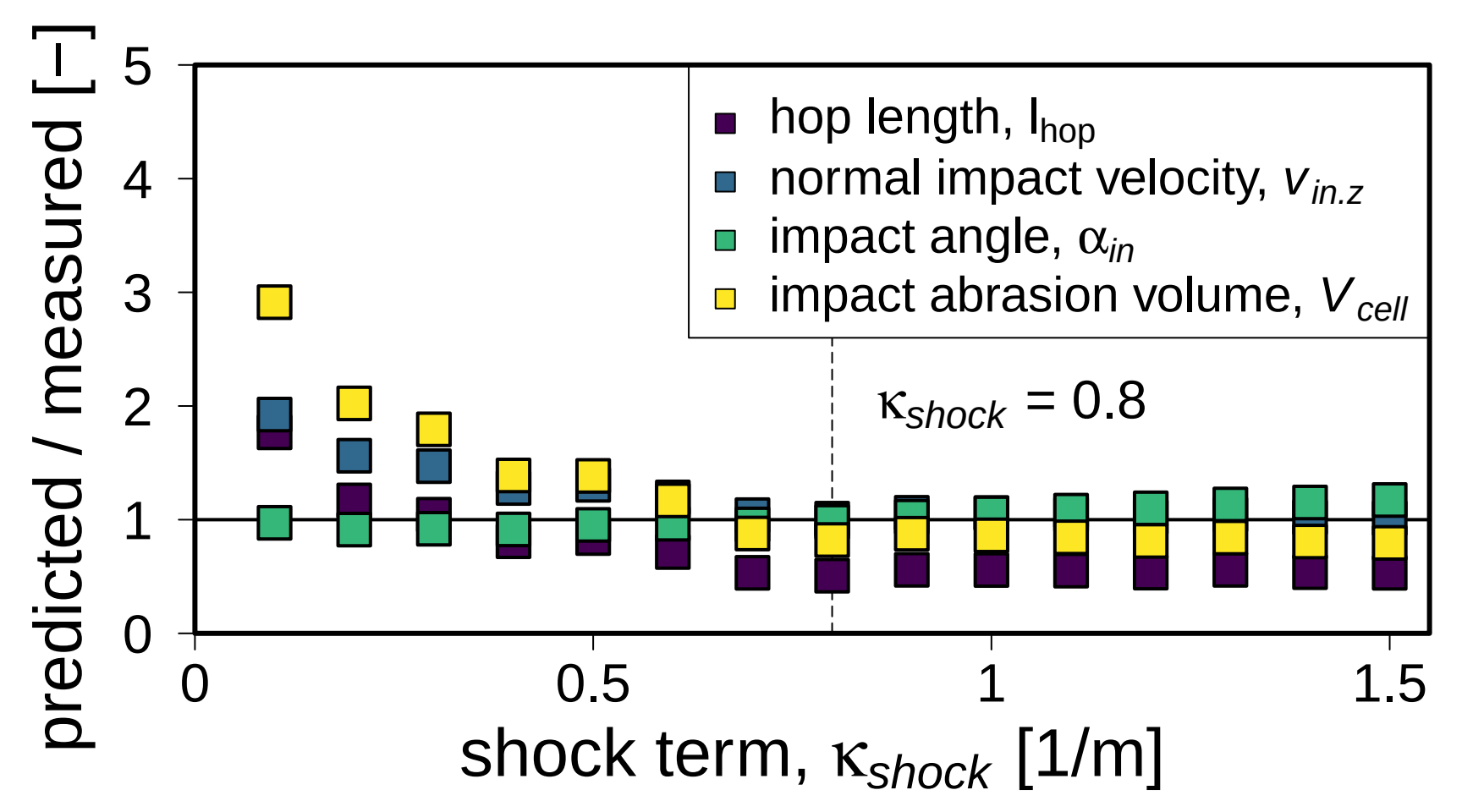
predicted / measured [–]
5
4
3
2
1
0
0
0.5
1
1.5
shock term, κ_{shock} [1/m]
hop length, l_{hop}
normal impact velocity, $v_{in.z}$
impact angle, α_{in}
impact abrasion volume, V_{cell}
κ_{shock} = 0.8

PIV−cam1
PIV−cam2
PIV−cam3
PIV measured data
DGA modelled data
A.
B.
C.
D.
E.
F.
G.
hop length l_{hop} [m]
vertical impact velocity $v_{in.z}$ [m/s]
impact velocity v_{in} [m/s]
deflection velocity v_{out} [m/s]
impact angle α_{in} [°]
deflection angle α_{out} [°]
abrasion volume V_{cell} [m^3]
flume slope angle, θ_{slope} [°]
flume slope angle, θ_{slope} [°]
downslope length of the flume, l_{flume} [m]

A.

B.

EB3
EB4
EB5
FB–FB6

EB5
FB4

DGAM round
DGAM angular

hop length l_{hop} [m]

impact velocity v_{in} [m/s]

impact angle α_{in} [°]

1:1 (foam bed)

abrasion volume per meter, V_{cell} [m^2]

abrasion volume V_{cell} [m^3]

$V_{cell} \sim 0.003\ d_{grain}^{3.5}$

$R^2 = 0.99$

slope angle, θ_{slope} [°]

grainsize, d_{grain} [m]

intial
intermediate
late
run time
cs1
lp
cs2
entering grains
normalized
number of
transported
grains []
cs3
bed elevation below initial surface [m]
bed elevation [m]
lateral distance [m]
A.
B.
cs1
cs2
cs3
$\theta_{slope} = 35°$
trough
rim
trough
rim
lp
distance downslope [m]
C.
D.